Present-Day Methane Shortwave Absorption Mutes Surface Warming Relative to Preindustrial Conditions

Robert J. Allen[1], Xueying Zhao[1,2,3], Cynthia A. Randles[4*], Ryan J. Kramer[5], Bjørn H. Samset[6] and Christopher J. Smith[7,8]

[1]Department of Earth and Planetary Sciences, University of California, Riverside, CA, USA.

[2]National Center for Atmospheric Research, Boulder, CO.

[3]Department of Earth and Planetary Science, The University of Texas at Austin, Austin, TX, USA.

[4]ExxonMobil Technology and Engineering Company, Annandale, NJ, USA
[*]now at UNEP International Methane Emission Observatory, Paris, France.

[5]NOAA Geophysical Fluid Dynamics Laboratory, Princeton, NJ.

[6]CICERO Center for International Climate and Environmental Research in Oslo, Oslo, Norway.

[7]School of Earth and Environment, University of Leeds, Leeds, UK.

[8]International Institute for Applied Systems Analysis (IIASA), Laxenburg, Austria.

Correspondence to: Robert J. Allen (rjallen@ucr.edu)

Short Summary:

Present-day methane shortwave absorption mutes 28% (7-55%) of the surface warming associated with its longwave absorption. The precipitation increase associated with the longwave radiative effects of the present-day methane perturbation is also muted by shortwave absorption but not significantly so. Methane shortwave absorption also impacts the magnitude of its climate feedback parameter, largely through the cloud feedback.

32 **Abstract**. Recent analyses show the importance of methane shortwave absorption,
33 which many climate models lack. In particular, Allen et al. (2023) used idealized
34 climate model simulations to show that methane shortwave absorption mutes up to
35 30% of the surface warming and 60% of the precipitation increase associated with
36 its longwave radiative effects. Here, we explicitly quantify the radiative and
37 climate impacts due to shortwave absorption of the present-day methane
38 perturbation. Our results corroborate that present-day methane shortwave
39 absorption mutes the warming effects of longwave absorption. For example, the
40 global mean cooling in response to the present-day methane shortwave absorption
41 is -0.10 ± 0.07 K, which offsets 28% (7-55%) of the surface warming associated
42 with present-day methane longwave radiative effects. The precipitation increase
43 associated with the longwave radiative effects of the present-day methane
44 perturbation (0.012 ± 0.006 mm d^{-1}) is also muted by shortwave absorption but
45 not significantly so (-0.008 ± 0.009 mm d^{-1}). The unique responses to methane
46 shortwave absorption are related to its negative top-of-the-atmosphere effective
47 radiative forcing but positive atmospheric heating, and in part methane's
48 distinctive vertical atmospheric solar heating profile. We also find that the present-
49 day methane shortwave radiative effects, relative to its longwave radiative effects,
50 are about five times larger than those under idealized carbon dioxide perturbations.
51 Additional analyses show consistent but non-significant differences between the
52 longwave versus shortwave radiative effects for both methane and carbon dioxide,
53 including a stronger (negative) climate feedback when shortwave radiative effects
54 are included (particularly for methane). We conclude by reiterating that methane
55 remains a potent greenhouse gas.

56
57
58
59
60
61
62
63
64
65
66
67
68
69
70
71

1 Introduction

Several recent studies (Li et al., 2010; Etminan et al., 2016; Collins et al., 2018; Byrom and Shine, 2022) have shown the significance of methane (CH_4) shortwave (SW) absorption—which is lacking in many climate models (Forster et al., 2021)—at near-infrared (NIR) wavelengths. Etminan et al. (2016) first showed methane SW absorption increases its stratospherically adjusted radiative forcing (SARF) by up to ~15% as compared to its longwave (LW) SARF. Smith et al. (2018) subsequently inferred negative rapid adjustments (i.e., surface temperature independent responses; see Section 2) due to CH_4 SW absorption, using four of ten models from the Precipitation Driver and Response Model Intercomparison Project (PDRMIP; Myhre et al., 2017) that included an explicit representation of methane SW absorption. Byrom and Shine (2022) showed that CH_4 SW forcing depends on several factors, including the spectral variation of surface albedo, the vertical profile of methane, and absorption of solar radiation at longer wavelengths, specifically methane's 7.6 µm band. They estimated a smaller impact of CH_4 SW absorption, with a 7% increase in SARF, in part due to the inclusion of the 7.6 µm band which mainly impacts stratospheric solar absorption.

The recent analysis of Allen et al. (2023) (hereafter referred to as A23) used Community Earth System Model version 2 (CESM2; Danabasoglu et al., 2020) simulations to isolate the effects of CH_4 SW absorption, and showed that it muted the surface warming and wetting due to methane's LW radiative effects. Muting of surface warming was attributed largely to cloud rapid adjustments, including increased low-level clouds and decreased high-level clouds. These cloud changes in turn were associated with the vertical profile of atmospheric solar heating, and corresponding changes to atmospheric temperature and relative humidity.

We adopt similar terminology as in A23. Throughout this manuscript, the terms "SW radiative effect"/"SW absorption" and "LW radiative effect" refers to the radiative effects of methane (and eventually carbon dioxide) on the climate system as isolated by a suite of simulations (to be discussed below). This terminology is used interchangeably with the abbreviations "CH_{4SW}" and "CH_{4LW}", respectively.

A23 focused on three idealized methane perturbations, including 2x, 5x and 10x preindustrial methane concentrations. Relatively large perturbations were emphasized to maximize the signal to noise ratio, as well as to robustly identify mechanisms. Despite these relatively large methane perturbations, 5x preindustrial methane concentrations are comparable to end of 21st century projections under the Shared Socioeconomic Pathway 3-7.0 (i.e., 0.75 ppm to 3.4 ppm). Although

112   5xCH4 and 10xCH4 SW radiative effects showed a clear muting of the
113   corresponding LW effects, 2xCH4 did not. For example, the global mean near-
114   surface air temperature (TAS) response under 5xCH4SW and 10xCH4SW yielded
115   significant global cooling at -0.23 ± 0.07 and -0.39 ± 0.07 K. We reiterate that
116   this cooling is due to isolation of methane shortwave absorption alone; the total
117   (including methane's longwave absorption) temperature response is significant
118   warming at 0.45 ± 0.05 and 0.85 ± 0.05 K, respectively (i.e., longwave
119   absorption effects dominate). 2xCH4SW, however, yielded a warming response of
120   0.06 ± 0.06 K that is not significant at the 90% confidence level. Similar results
121   apply for the global mean precipitation (P) response, where a significant decrease
122   occurred under 5xCH4SW and 10xCH4SW at -0.021 ± 0.008 and $-0.039 \pm$
123   0.008 mm d^{-1} (-0.7 and -1.3%). For 2xCH4SW, the response was again not
124   significant at 0.002 ± 0.008 mm d^{-1} (0.06%). The lack of significant climate
125   responses in the 2xCH4SW coupled ocean-atmosphere simulation is consistent with
126   its relatively weak forcing as compared to the larger methane perturbations, and
127   relative to internal climate variability of the coupled ocean-atmosphere system.
128
129   Here we conduct analogous simulations as A23 to explicitly calculate the
130   shortwave absorption effects of the present-day methane concentration, i.e., the
131   ~750 to ~1900 ppb increase (~2.5x). Our results support the prior conclusions
132   from A23. We further expand upon our understanding of the climate effects of
133   CH4SW by conducting an atmospheric energy budget analysis and by evaluating the
134   climate feedback and hydrological sensitivity parameters (and climate sensitivity),
135   and by comparing the effects of methane SW absorption with those from carbon
136   dioxide SW absorption.
137
138   **2 Materials and Methods**
139
140   An array of targeted methane-only and carbon dioxide-only equilibrium time slice
141   (i.e., cyclic repetition of the imposed perturbation) climate simulations are
142   conducted with CESM2 (Danabasoglu et al., 2020), which includes the most recent
143   model components such as the Community Atmosphere Model version 6 (CAM6).
144   CAM6's radiation parameterization, the Rapid Radiative Transfer Model for
145   general circulation models (RRTMG; Iacono et al., 2008) includes a representation
146   of CH4 SW absorption in three near-infrared bands including 1.6-1.9 μm, 2.15-2.50
147   μm and 3.10-3.85 μm. Methane shortwave absorption at 7.6 μm (the mid-infrared;
148   mid-IR), however, is not represented. Furthermore, although CESM2 includes a
149   representation of CH4 SW absorption, RRTMG underestimates CH4 (and CO2) SW
150   IRF by 25-45% (Hogan and Matricardi, 2020).

151   Our focus here is a set of 2.5x preindustrial atmospheric CH_4 concentration
152   simulations, to complement the three methane perturbations (2x, 5x and 10x
153   preindustrial atmospheric CH_4 concentrations) performed by A23. We perform
154   both fixed climatological sea surface temperatures (fSST) and fully coupled ocean-
155   atmosphere simulations (Table 1), and conduct two sets of identical experiments,
156   one that includes CH_4 LW+SW radiative effects ($2.5xCH_4^{EXP}$) and one that lacks
157   CH_4 SW radiative effects ($2.5xCH_{4NOSW}^{EXP}$). CH_4 SW absorption in the three NIR
158   bands in RRTMG is turned off in the simulations that lack methane SW
159   absorption. These are compared to a default preindustrial control experiment
160   (PIC^{EXP}), which includes CH_4 (as well as other radiative species such as CO_2)
161   LW+SW radiative effects, as well as to a preindustrial control experiment with
162   CH_4 SW radiative effects turned off (i.e., LW effects only, denoted as
163    $PIC_{NOCH4SW}^{EXP}$). To clarify, SW changes can still be present in $2.5xCH_{4NOSW}^{EXP}$, but
164   only as a rapid adjustment (or a temperature-induced response) associated with the
165   direct LW absorption of methane. For example, direct LW absorption of methane
166   can drive changes in water vapor and clouds, which in turn could impact SW
167   radiation.

168   This suite of CH_4 simulations allows quantification of the CH_4 LW+SW, LW and
169   SW radiative effects, denoted as $2.5xCH_{4LW+SW}$, $2.5xCH_{4LW}$ and $2.5xCH_{4SW}$. The
170    $2.5xCH_{4LW+SW}$ signal is obtained by subtracting the default $2.5xCH_4$ perturbation
171   from the default control ($2.5xCH_4^{EXP} - PIC^{EXP}$). The $2.5xCH_{4LW}$ signal is
172   obtained by subtracting the $2.5xCH_4$ perturbation without CH_4 SW absorption from
173   the corresponding control simulation without CH_4 SW absorption
174   ($2.5xCH_{4NOSW}^{EXP} - PIC_{NOCH4SW}^{EXP}$). The $2.5xCH_{4SW}$ signal is obtained by taking the
175   double difference, i.e., ($2.5xCH_4^{EXP} - PIC^{EXP}$) $-$ ($2.5xCH_{4NOSW}^{EXP} -$
176    $PIC_{NOCH4SW}^{EXP}$). The $2.5xCH_{4SW}$ signal therefore represents CH_4 SW absorption and
177   also the impacts of this SW absorption on CH_4 LW rapid adjustments (and surface
178   temperature responses). We also calculate the corresponding instantaneous
179   radiative forcing (IRF), which is defined as the initial perturbation to the radiation
180   balance, using the Parallel Offline Radiative Transfer (PORT) model (Conley et
181   al., 2013). PORT isolates the RRTMG radiative transfer computation from the
182   CESM2-CAM6 model configuration.

183   Fixed SST experiments are used to estimate the 'fast' climate responses and the
184   effective radiative forcing (ERF). ERF is defined as the top-of-the-atmosphere
185   (TOA) net radiative flux difference between the experiment and control simulation,
186   with climatological fixed SSTs and sea-ice distributions without any adjustments
187   for changes in the surface temperature over land (Forster et al., 2016). ERF can be
188   decomposed into the sum of the IRF and rapid adjustments (ADJs). Rapid

189 adjustments represent the change in state in response to the initial perturbation (i.e.,
190 IRF) excluding any responses related to changes in sea surface temperatures. Rapid
191 adjustments, which for example include clouds and water vapor, are estimated
192 using the radiative kernel method (Soden et al., 2008; Smith et al., 2018, 2020)
193 applied to the climatological fixed SST simulations. A radiative kernel is basically
194 the partial derivative of the radiative flux with respect to a variable (e.g., moisture)
195 that changes with temperature. It therefore represents the radiative impacts from
196 small perturbations in a state. To calculate the rapid adjustments, the radiative
197 kernel is multiplied by the change in the climate variable under consideration
198 (from the fSST simulations). The Python-based radiative kernel toolkit of Soden et
199 al. (2008), along with the Geophysical Fluid Dynamics Laboratory radiative
200 kernel, are used here. The method for calculating cloud rapid adjustments with
201 radiative kernels is a bit more involved. Here, we use the kernel difference method
202 (Smith et al., 2018) which employs a cloud-masking correction applied to the
203 cloud radiative-forcing diagnostics. The cloud-masking correction is based on the
204 kernel-derived non-cloud adjustments and IRF. A23 showed that this methodology
205 performed well, including a small residual term (i.e., $ERF - IRF - \Sigma ADJs <$
206 $\sim 5\%$ of ERF). Furthermore, similar results were obtained with an alternative
207 radiative kernel based on CloudSat/CALIPSO (Kramer et al., 2019).

208 The total climate response, which includes the IRF, ADJs and the surface
209 temperature responses, is quantified using the coupled ocean-atmosphere
210 experiments. Specifically, the radiative effects associated with the total climate
211 response are estimated using the same radiative kernel decomposition as above, but
212 applied to the coupled ocean-atmosphere simulation. The surface temperature
213 responses (i.e., 'slow' response) are estimated as the difference between the
214 coupled ocean atmosphere simulations and the climatologically fixed SST
215 experiments. Similarly, the radiative effects associated with the slow response are
216 calculated as the difference between the kernel-derived radiative effects of the total
217 and fast responses.

218 To reiterate, our framework is to decompose the total response (directly estimated
219 from coupled simulations) into a fast (surface temperature independent) response
220 and a slow (surface temperature dependent) response:

221   Total Response = Fast Response + Slow Response   (1)

222 The fast response is directly estimated from the fSST simulations and includes the
223 rapid adjustments. The slow response is estimated from the difference of the total
224 and fast responses (i.e., coupled simulation minus fSST simulation). This is
225 consistent with the IPCC framework, which uses the concepts of an adjustment to

226 an imposed forcing (i.e., independent of surface temperature) and a radiative
227 response to a global mean temperature change. It is also analogous to the
228 methodology employed in several other papers, including many PDRMIP papers
229 (e.g., Samset et al., 2016; Myhre et al., 2017).

230 Our simulations are performed at 1.9° x 2.5° latitude-longitude resolution with 32
231 atmospheric levels. Coupled ocean-atmosphere experiments are initialized from a
232 spun-up preindustrial control simulation and subsequently integrated for 90 years.
233 Total climate responses are estimated using the last 40 years of these coupled
234 ocean-atmosphere experiments. As climatologically fixed SST simulations
235 equilibrate more quickly, these are run for 32 years. The ERF and rapid
236 adjustments are estimated from the last 30 years of these fSST experiments.

237 Our integration lengths are consistent with other related idealized time-slice studies
238 including for example a 100-year integration (and analysis of the last 50 years) of
239 coupled simulations under PDRMIP (e.g., Samset et al., 2016; Myhre et al., 2017).
240 A similar statement applies for the integration length of our fSST runs, e.g., the
241 Radiative Forcing Model Intercomparison Project (RFMIP; Pincus et al., 2016)
242 specifies 30-year fSST simulations.

243 We note that even with a 90-year coupled ocean simulation, the model has not yet
244 reached equilibrium. Given computational resource limitations, there is always a
245 tradeoff between the number of simulations performed and length of each
246 simulation.
247

248 A two-tailed pooled t test is used to assess the statistical significance of a climate
249 response, based on the annual mean difference between the experiment and
250 control. We evaluate a null hypothesis of zero difference with $n_1 + n_2 - 2$ degrees
251 of freedom. Here, n_1 and n_2 are the number of years in the experiment and control
252 simulations (e.g., 40 years for the coupled ocean-atmosphere runs). The pooled
253 variance $S_p^2 = \frac{(n1-1)S_1^2 + (n2-1)S_2^2}{n1+n2-2}$ is used, where S_1^2 and S_2^2 are the sample variances.
254 Quoted uncertainty estimates are based on the 90% confidence interval using the
255 pooled variance according to 1.65*S_p.

256

257 **3 Results**

258 **3.1 2.5xCH$_4$ Radiative Flux Components & Rapid Adjustments**

259 Figure 1a shows the 2.5xCH$_4$ TOA ERF, IRF and ADJ, as well as the radiative
260 kernel decomposition of ADJ (Fig. 1b). The 2.5xCH$_4$ TOA LW IRF is $0.46 \pm$
261 0.05 W m^{-2} and the corresponding TOA SW IRF is 0.06 ± 0.07 W m^{-2} (not
262 significant at the 90% confidence level).

264 The 2.5xCH$_4$ instantaneous shortwave heating rate (QRS) profile (Figure 2a)
265 exhibits positive values for atmospheric pressure levels less than ~700 hPa and
266 negative values for pressure levels greater than ~700 hPa. As discussed in A23,
267 increasing the atmospheric methane concentration does not increase lower-
268 tropospheric SW heating because the three near-infrared bands are already highly
269 saturated here (e.g., due to water vapor absorption). Furthermore, the methane-
270 induced QRS increase aloft decreases the available solar radiation in the three
271 near-IR methane absorption bands (1.6-1.9 μm, 2.15-2.50 μm and 3.10-3.85 μm)
272 that can be absorbed by other gases (e.g., water vapor) in the lower-troposphere.
273 This results in the decrease in SW heating-rate in the lower troposphere (Fig. 2a).
274 Both of these features exist under 2.5xCH$_{4SW}$ and are consistent with the other
275 methane perturbations, with the larger perturbations (e.g., 5xCH$_{4SW}$), yielding
276 larger QRS increases aloft and larger QRS decreases in the lower troposphere.

278 As mentioned above, A23 showed that methane SW radiative effects lead to a
279 negative rapid adjustment (largely due to changes in clouds) that acts to cool the
280 climate system. A positive ADJ represents a net energy increase, whereas a
281 negative ADJ represents a net energy decrease. Individual rapid adjustments, as
282 well as the total adjustment, under 2.5xCH$_4$ are displayed in Figure 1b. Under
283 2.5xCH$_{4SW}$, the total rapid adjustment is -0.16 ± 0.10 W m^{-2}, which is largely due
284 to the cloud adjustment at -0.12 ± 0.08 W m^{-2}. The stratospheric temperature
285 adjustment contributes the remainder at -0.04 ± 0.01 W m^{-2}. The remaining terms
286 (i.e., surface temperature, tropospheric temperature, surface albedo and water
287 vapor adjustments), most of which are not significant at the 90% confidence level,
288 have a net zero contribution to the total adjustment (i.e., their sum is zero). Thus,
289 similar to the larger CH$_4$ perturbations in A23, 2.5xCH$_{4SW}$ yields a significant
290 negative total rapid adjustment that is largely due to the cloud adjustment.

291 This negative rapid adjustment promotes a negative ERF under methane SW
292 absorption. We reiterate that the negative ERF is due to isolation of methane
293 shortwave absorption alone; methane's longwave effects still dominate the ERF.
294 This is because the ERF is the sum of ADJs and IRF. For example, under the larger
295 5xCH$_{4SW}$ perturbation in A23, the ERF and ADJ were both significant at $-0.22 \pm$
296 0.17 W m^{-2} and -0.36 ± 0.13, respectively. Under 2.5xCH$_{4SW}$, the ERF and ADJ
297 (Fig. 1a) are -0.10 ± 0.13 W m^{-2} and -0.16 ± 0.10 W m^{-2}, respectively, with the

298 latter significant at the 90% confidence level.   As with the larger methane
299 perturbations, 2.5xCH$_{4SW}$ offsets (although not significantly so) ~20% of the ERF
300 associated with 2.5xCH$_{4LW}$ (0.53 ± 0.11 W m^{-2}).

301 The corresponding surface CH$_{4SW}$ "ERFs" (not shown) are more negative than
302 those at the TOA, at -0.18 ± 0.10 W m^{-2} for 2.5xCH$_{4SW}$ (significant at the 95%
303 confidence interval). We note that technically this is not an ERF, but we retain this
304 terminology since it is calculated analogously to ERF, just using surface as
305 opposed to TOA radiative fluxes. This negative surface ERF is consistent with
306 negative surface CH$_{4SW}$ IRF values (due to atmospheric solar absorption, which
307 decreases surface solar radiation), and the vertical redistribution of shortwave
308 heating (Fig. 2a) that drives a negative surface rapid adjustment that is again
309 largely due to the cloud adjustment. The surface 2.5xCH$_{4SW}$ IRF value is $-0.10 \pm$
310 0.05 W m^{-2} and the corresponding sum of the surface rapid adjustments is
311 -0.08 ± 0.07 W m^{-2} (not shown).
312
313
314 **3.2 2.5xCH$_{4SW}$ Fast Climate Response**
315
316 Figure 2b-f shows global mean vertical response profiles from the fSST
317 simulations for the four methane shortwave absorption perturbations (e.g.,
318 2.5xCH$_{4SW}$). 2.5xCH$_{4SW}$ yields QRS increases (Fig. 2b) in the upper
319 troposphere/lower stratosphere, as well as QRS decreases in the lower-troposphere.
320 This is consistent with the aforementioned instantaneous QRS profile response
321 (Fig. 2a). These changes are associated with temperature (Fig. 2c) and relative
322 humidity (RH; Fig. 2d) changes that favor increases in low-level cloud cover
323 (CLOUD; Fig. 2e) that peak near 800 hPa and decreases in high-level cloud cover
324 (e.g., for pressures < 300 hPa). Both of these CLOUD responses act to cool the
325 surface. These cloud changes become larger under the larger methane
326 perturbations. For example, 2.5xCH$_{4SW}$ yields a decrease in global mean lower-
327 tropospheric (pressures > 800 hPa) temperature of -0.02 ± 0.02 K (not significant
328 at the 90% confidence level) and an increase in upper-tropospheric (between 100
329 and 500 hPa) temperature of 0.09 ± 0.04 K (significant at the 95% confidence
330 level). Similarly, global mean lower-tropospheric RH increases by 0.01 ± 0.06 %
331 and upper-tropospheric RH decreases by -0.09 ± 0.10 % (however, both changes
332 are not significant at the 90% confidence level). Global mean lower-tropospheric
333 CLOUD increases by 0.045 ± 0.04 % (low cloud as quantified in CESM2 yields
334 0.08 ± 0.07%; Supplementary Table 1) and upper-tropospheric CLOUD decreases
335 by -0.07 ± 0.04 %.

336   Correlations between the $2.5xCH_{4SW}$ global mean vertical response profiles are
337   significant. For example, the correlation between the global mean vertical
338   temperature and QRS response profile from 990 hPa to 100 hPa is 0.93. The
339   corresponding correlation between temperature and RH is -0.89, and the
340   corresponding correlation between RH and CLOUD is 0.80. Thus, an increase in
341   SW heating is associated with warming whereas a decrease in SW heating is
342   associated with cooling. Warming is associated with a decrease in RH whereas
343   cooling is associated with an increase in RH. Furthermore, an increase in RH is
344   associated with an increase in CLOUD whereas a decrease in RH is associated
345   with a decrease in CLOUD. These results help to support the importance of
346   atmospheric SW absorption in driving the CLOUD response through altered
347   temperature and RH. Spatial correlations at specific pressure levels also yield
348   similarly significant but somewhat weaker correlations (Supplementary Figure 1).
349   For example, spatially correlating the global mean annual mean change in CLOUD
350   with the corresponding change in RH yields significant correlations in the lower-
351   troposphere ranging from 0.40 to 0.65, as well as in the upper-troposphere ranging
352   from 0.71 to 0.81. Similar conclusions are obtained with the larger methane
353   perturbations.

354   These cloud changes are similar to those that occur in response to absorbing
355   aerosols like black carbon (i.e., the aerosol-cloud semi-direct effect; Amiri-
356   Farahani et al., 2019; Allen et al., 2019). Black carbon solar heating warms and
357   dries (decreased relative humidity) the free troposphere, which promotes less cloud
358   cover in the mid- to upper-troposphere (Stjern et al., 2017). Warming aloft (and
359   cooling of the lower troposphere under CH_{4SW}) also suggest enhanced lower-
360   tropospheric stability. As lower-tropospheric stability is a measure of the inversion
361   strength that caps the boundary layer, enhanced lower-tropospheric stability traps
362   more moisture in the marine boundary layer, allowing for enhanced cloud cover
363   (e.g., Wood and Bretherton, 2006). Under $2.5xCH_{4SW}$, global mean lower-
364   tropospheric stability (estimated here as the temperature difference between 600
365   hPa and 990 hPa) significantly increases (at the 95% confidence level) by $0.03 \pm$
366   0.02 K. Larger increases in lower-tropospheric stability occur under the larger
367   methane perturbation, e.g., 0.06 ± 0.02 K under $10xCH_{4SW}$ (and similarly, larger
368   increases in low clouds occur at $0.36 \pm 0.10\%$; Supplementary Table 1). This
369   increase in low cloud cover, most of which occurs over the oceans (Supplementary
370   Figure 2a,d,g,j), is consistent with the increase in lower-tropospheric stability.
371   Furthermore, enhanced stability also suggests reduced convective mass flux in the
372   mid/upper-troposphere. Although we did not archive convective mass flux, Fig. 2f
373   shows changes in convective cloud cover (CONCLOUD). All methane
374   perturbations show decreased CONCLOUD in the mid/upper troposphere

375 (pressures < 800 hPa). CONCLOUD also increases in the lower-troposphere
376 (peaking near 900 hPa). Although these CONCLOUD changes are weaker than
377 those associated with CLOUD, their profiles are very similar, implying that
378 changes in convection also contribute to changes in CLOUD.

379
380 **3.3 2.5xCH$_{4SW}$ Total Climate Response**
381
382 Figure 3a-e shows global mean vertical total climate response profiles from the
383 coupled ocean-atmosphere simulations for the four methane shortwave absorption
384 perturbations (e.g., 2.5xCH$_{4SW}$). The QRS, RH and CLOUD responses are similar
385 to those from the fSST simulation (Fig. 2), which further highlights the importance
386 of rapid adjustments to the total climate response. For example, similar to the fast
387 response, the total response features increases in low- and mid-level clouds (Fig.
388 3c; peaking near 800 hPa) and decreases in high-level clouds (for pressures < 300
389 hPa) occurs, both of which act to cool the surface (Fig. 3f).
390
391 Relative to the fast responses discussed above, the total responses are generally
392 similar but larger and more significant in the lower (and mid) troposphere but
393 weaker in the upper troposphere. This is consistent with allowing the surface to
394 respond to the CH$_{4SW}$ perturbation in the fully coupled ocean-atmosphere
395 experiments, and in particular, the negative surface CH$_{4SW}$ "ERFs" discussed in
396 Section 3.1 (i.e., decrease in surface solar radiation). For example, the 2.5xCH$_{4SW}$
397 total response features a decrease in global mean lower-tropospheric temperature
398 (Fig. 3b) of -0.10 ± 0.07 K which is significant at the 95% confidence level and
399 about 5x as large as the cooling under the fast response (Fig. 2c). This smaller
400 lower-tropospheric temperature adjustment (i.e., fast response) is consistent with
401 the experimental design (i.e., fixed SSTs). A non-significant decrease in upper-
402 tropospheric temperature of -0.02 ± 0.11 K occurs under the total response, in
403 contrast to the upper-tropospheric warming under the fast response (Fig. 2c).
404 Similarly, global mean lower-tropospheric RH (Fig. 3d) increases by 0.05 ± 0.05
405 % (significant at the 90% confidence level) under the 2.5xCH$_{4SW}$ total response,
406 with a non-significant change in upper-tropospheric RH of -0.02 ± 0.08 %.
407 Global mean lower-tropospheric CLOUD (Fig. 3c) increases by 0.12 ± 0.07 %
408 (significant at the 99% confidence level) and upper-tropospheric CLOUD
409 decreases by -0.06 ± 0.03 % (significant at the 99% confidence level). The
410 corresponding changes under the fast response (Fig. 2) are generally similar, but
411 smaller in the lower-troposphere (i.e., smaller increases in RH and CLOUD) but
412 larger in the upper-troposphere (i.e., larger decreases in RH and CLOUD). The
413 total response of CONCLOUD (Fig. 3e) is generally similar to the fast response

414   (Fig. 2f), although the 2.5xCH$_{4SW}$ total response lacks an increase in the lower-
415   troposphere.
416
417   Global maps of the TAS and P total climate responses (from coupled ocean-
418   atmosphere simulations) under 2.5xCH$_{4SW}$ are shown in Fig. 3f,g. The global mean
419   TAS response is -0.10 ± 0.07 K (significant at the 95% confidence level); the
420   global mean P response is -0.008 ± 0.009 mm d^{-1} (-0.27%) which is not
421   significant at the 90% confidence level. Comparing these 2.5xCH$_{4SW}$ responses to
422   the corresponding 2.5xCH$_{4LW}$ responses of 0.36 ± 0.05 K and 0.012 ± 0.006 mm
423   d^{-1} shows that under 2.5xCH$_4$, methane shortwave absorption offsets 28% (7-55%)
424   of the surface warming and 66% of the precipitation increase associated with its
425   longwave radiative effects. Although the 66% muting of the precipitation increase
426   is not significant, this percentage is qualitatively consistent with the larger methane
427   perturbations.
428

429   As noted in Section 3.1, consistent with the larger methane perturbations, the
430   2.5xCH$_{4SW}$ ERF at 0.10 ± 0.13 W m^{-2} offsets 19% (although not significant) of the
431   ERF associated with 2.5xCH$_{4LW}$. In contrast, 2.5xCH$_{4SW}$ offsets a larger
432   percentage of the surface warming associated with 2.5xCH$_{4LW}$ at 28%. Based on
433   the global mean TOA energy decomposition equation $\Delta N = \Delta F + \alpha \Delta TAS$ (e.g.,
434   Forster et al., 2021), where ΔN is the change in the global mean TOA net energy
435   flux [W m^{-2}]; ΔTAS is the change in global mean near-surface air temperature [K];
436   ΔF is the change in the global mean TOA net energy flux [W m^{-2}] when $\Delta TAS = 0$
437   (i.e., the effective radiative forcing, ERF); and α is the net feedback parameter [W
438   m^{-2} K^{-1}], if ΔF is reduced by X%, ΔTAS should also be reduced by X% assuming a
439   constant α. Supplementary Table 2 and Supplementary Figure 3 show the
440   individual components of the TOA energy decomposition equation, including the
441   estimated climate feedback parameter (details on how these are calculated are
442   included in the corresponding captions). The climate feedback parameter is always
443   larger (in magnitude) under the various SW+LW signals (e.g., 2.5xCH$_{4LW+SW}$) as
444   compared to the LW-only signal (e.g., 2.5xCH$_{4LW}$), which suggests the climate
445   system does not have to warm as much to offset the same TOA energy imbalance
446   when SW effects are included. However, α has a relatively large uncertainty and it
447   is not significantly different between the various SW+LW signals and the
448   corresponding LW-only signals. For example, the climate feedback parameter is
449   -1.80 ± 0.44 W m^{-2} K^{-1} for 10xCH$_{4LW+SW}$ and -1.45 ± 0.26 W m^{-2} K^{-1} for
450   10xCH$_{4LW}$. The SW signal consistently (outside of 2.5xCH$_{4SW}$) yields the smallest
451   (negative) α. The corresponding value for 10xCH$_{4SW}$ is -0.73 ± 1.08 W m^{-2} K^{-1}.

452 We also note that the 2.5xCH$_{4SW}$ α has an unphysical positive value (but again
453 with large uncertainty) at 0.87 ± 3.41 W m^{-2} K^{-1}. Thus, the climate feedback
454 parameter is not significantly different under the LW-only effects versus SW
455 effects of CH$_4$. This uncertainty also helps to explain why the SW effect
456 contributes different percentages (which are not significant under 2.5xCH$_4$) for
457 ERF and ΔTAS. Additional analyses (Section 3.7), however, show that there are
458 significant differences in the cloud feedback (largely due to low clouds) that lend
459 additional support to the notion that the climate feedback parameter is different
460 (less negative) under methane SW radiative effects.

461 Analogous conclusions exist for the climate sensitivity parameter λ (K [W m^{-2}]$^{-1}$;
462 i.e., $-1 \times \alpha^{-1}$). λ is consistently smaller under the various SW+LW signals
463 relative to the corresponding LW-only signals (Supplementary Table 2), implying
464 less warming in response to the same TOA energy imbalance when SW effects are
465 included. The SW signal (outside of 2.5xCH$_{4SW}$) consistently yields the largest λ,
466 implying relatively large temperature change in response to the same TOA energy
467 imbalance. Again, however, the uncertainty is large and these differences are not
468 significant. For example, the climate sensitivity parameter is 0.55 ± 0.13 K [W m^{-2}]$^{-1}$ under 10xCH$_{4LW+SW}$ versus 0.69 ± 0.12 K [W m^{-2}]$^{-1}$ under 10xCH$_{4LW}$. The
469 corresponding λ under 10xCH$_{4SW}$ is 1.37 ± 2.02 K [W m^{-2}]$^{-1}$.

471
472 **3.4 2.5xCH$_{4SW}$ Slow Climate Response**

473 We apply the radiative kernel decomposition to the 2.5xCH$_{4SW}$ coupled ocean-
474 atmosphere simulation (Figure 4; Supplementary Figure 4 shows the corresponding
475 results for 2.5xCH$_{4SW+LW}$ and 2.5xCH$_{4LW}$). The 'fast' responses from the fixed
476 climatological SST runs (i.e., the rapid adjustments) and the surface-temperature-
477 induced 'slow' responses (i.e., the difference between the coupled ocean
478 atmosphere and fixed climatological SST simulations) are also included. Here, a
479 positive slow response has the same meaning as a positive fast response (ADJ), as
480 both represent a net energy increase. Similarly, a negative slow response has the
481 same meaning as a negative ADJ, as both represent a net energy decrease (i.e., we
482 do not normalize by the change in surface air temperature as is done to calculate a
483 climate feedback). As with the larger methane perturbations, the cloud rapid
484 adjustment and the cloud slow response under 2.5xCH$_{4SW}$ are both negative at
485 -0.12 ± 0.08 W m^{-2} and -0.28 ± 0.18 W m^{-2}, respectively. Both are consistent
486 with an increase in low cloud cover (particularly the slow response at $0.31 \pm$
487 0.25%; Supp. Table 1). This implies that surface cooling in response to
488 2.5xCH$_{4SW}$ radiative effects is largely due to the cloud rapid adjustment and cloud

13

489   slow responses.

490   As mentioned in Section 3.1, the $2.5xCH_{4SW}$ stratospheric temperature adjustment
491   under fixed climatological SSTs also significantly contributes (at -0.04 ± 0.01 W
492   m^{-2}; about 1/3 the magnitude of the cloud adjustment) to the total rapid adjustment.
493   This negative stratospheric temperature adjustment is consistent with the relatively
494   large increase in stratospheric shortwave heating (Fig. 2b) and warming (Fig. 2c),
495   which results in enhanced outgoing longwave radiation (i.e., loss of energy and a
496   negative adjustment).   The tropospheric temperature adjustment (Fig. 4) is also
497   negative but not significant at the 90% confidence level at -0.03 ± 0.05 W m^{-2}.
498   In contrast, the surface temperature adjustment at 0.02 ± 0.01 W m^{-2} (associated
499   with cooling of the land surfaces and subsequent reduction in upwards longwave
500   radiation) acts to weakly mute the negative total rapid adjustment. The other
501    $2.5xCH_{4SW}$ rapid adjustment components (e.g., tropospheric temperature, water
502   vapor, surface albedo) are relatively small and not significant at the 90%
503   confidence level.

504   In terms of the $2.5xCH_{4SW}$ slow response, in addition to the dominant negative
505   contribution from clouds, the water vapor and surface albedo slow response also
506   contribute to the negative total slow response at -0.09 ± 0.12 and -0.035 ± 0.03
507   W m^{-2}, respectively (Fig. 4).   These are associated with tropospheric/surface
508   cooling, resulting in less water vapor (a greenhouse gas) and enhanced snow/ice
509   over land (enhanced albedo). In contrast, the tropospheric temperature and surface
510   temperature slow responses are both significant and positive at 0.25 ± 0.19 and
511   0.05 ± 0.04 W m^{-2}, respectively, and act to mute the total negative slow response
512   (the stratospheric temperature adjustment also weakly contributes to this muting at
513   0.01 ± 0.01 W m^{-2}).

514   We note that the $2.5xCH_{4SW}$ total radiative flux decomposition (sum over clouds,
515   water vapor, etc.) for the slow response is negative (opposite expectations since the
516   surface cools). However, there is large uncertainty, i.e., it is a nonsignificant
517   negative value at -0.10 ± 0.30 W m^{-2}. This number is based on the corresponding
518   difference between the coupled ocean atmosphere total response and the rapid
519   adjustment from the fSST simulation, which have values of -0.27 ± 0.28 W m^{-2}
520   and -0.16 ± 0.10 W m^{-2}, respectively. The former number (-0.27 ± 0.28 W m^{-2})
521   is based on the total radiative flux decomposition under $2.5xCH_{4SW+LW}$ minus
522    $2.5xCH_{LW}$, which have respective values of -0.46 ± 0.18 W m^{-2} and $-0.19 \pm$
523   0.19 W m^{-2}. So here, both values are negative, as expected (i.e., the system
524   responds to the positive forcing by warming and emitting more energy to space,
525   consistent with a stable climate system). It is likely longer integrations (beyond 90

526 years) are necessary to reduce the relatively large uncertainty in some of these
527 values.

528 Decomposing the 2.5xCH$_{4SW}$ cloud rapid adjustment into shortwave and longwave
529 radiation components (not shown), we find the cloud rapid adjustment for
530 shortwave radiation is -0.08 ± 0.08 W m^{-2} and the cloud adjustment for longwave
531 radiation is -0.05 ± 0.03 W m^{-2}. Thus, both shortwave and longwave cloud
532 radiative components contribute similarly to the negative cloud rapid adjustment.
533 Decomposing the slow cloud response into shortwave and longwave radiation
534 components, we find corresponding values of -0.33 ± 0.17 and 0.05 ± 0.05 W
535 m^{-2}, respectively. Here, the negative cloud slow response is largely due to cloud
536 shortwave radiative effects (consistent with the low cloud increase of $0.31 \pm$
537 0.25%; Supp. Table 1), which is partially muted by cloud longwave radiative
538 effects. These changes are qualitatively consistent with the 2.5xCH$_{4SW}$ CLOUD
539 changes discussed in Section 3.3, under the broad assumption that low clouds
540 primarily reflect shortwave radiation and high clouds primarily inhibit outgoing
541 longwave radiation. 2.5xCH$_{4SW}$ CLOUD changes under the fast response (Fig. 2e)
542 are augmented in the upper-troposphere (larger decreases in high-level cloud) as
543 compared to the total response (Fig. 3c) and in particular as compared to the slow
544 (Supplementary Figure 5c; Supplementary Figure 6d) response. The weaker
545 decrease in upper-level clouds under the slow response is consistent with a lack of
546 an increase in upper-tropospheric shortwave heating rate (Supplementary Fig. 6a).
547 These statements are clearer under 10xCH$_{4SW}$ (Supplementary Figure 5i;
548 Supplementary Figure 7).
549
550 In contrast, CLOUD changes under the total response (and the slow response) are
551 augmented in the low to mid-troposphere (larger increases in low to mid-level
552 cloud) as compared to the fast response. The larger increase in low-level cloud
553 under the slow response (most of which occurs over marine stratocumulus regions
554 off the North and South American western coasts; Supplementary Figure 5a,d,g,j)
555 is consistent with a low-level cloud positive feedback i.e., surface cooling
556 promotes more low clouds and in turn, more cooling, etc. (Clement et al., 2009;
557 Zelinka et al., 2020).
558

559 To summarize, we find that the shortwave absorption associated with the present-
560 day methane perturbation (2.5xCH$_4$) offsets 28% (7 to 55%) of the surface
561 warming associated with its longwave radiative effects. Similarly, although not
562 significant, methane shortwave absorption associated with the present-day
563 perturbation mutes 19% of the positive ERF under methane longwave radiative

564 effects; and 66% of the precipitation increase is offset. These responses are
565 associated with changes in the vertical profiles of shortwave heating (i.e., increases
566 for pressures < 700 hPa and decreases for pressures > 700 hPa) which impacts
567 atmospheric temperature, relative humidity and cloud cover. Although some of the
568 $2.5xCH_{4SW}$ results lack significance at the 90% confidence level (e.g., the total
569 precipitation response) they are qualitatively consistent with the results based on
570 the larger $5xCH_4$ and $10xCH_4$ perturbations showed in A23 (where, for example,
571 the total precipitation response is significant). The lack of more significant signals
572 under $2.5xCH_{4SW}$ is due to the weaker perturbation relative to internal climate
573 variability. However, the consistency of the $2.5xCH_{4SW}$ signals relative to those
574 under the larger methane perturbations ($5xCH_{4SW}$ and $10xCH_{4SW}$) supports the
575 robustness of the main conclusions regarding the importance of methane SW
576 absorption.

577 **3.5 Additional Analysis of the Precipitation Response**
578
579 Precipitation responses can be understood from an energetic perspective (Muller
580 and O'Gorman, 2011; Richardson et al., 2016; Liu et al., 2018). Precipitation is
581 related to the diabatic cooling and the dry static energy flux divergence of the
582 atmosphere as $L_cP = Q + H$, where L_c is the latent heat of condensation of water
583 vapor; P is precipitation; Q is the column integrated diabatic cooling of the
584 atmosphere excluding latent heating; and H is the column integrated dry static
585 energy flux divergence. Q is estimated as LWC + SWC + SH. LWC is the net
586 longwave radiative cooling of the atmosphere. SWC is the net shortwave radiative
587 cooling of the atmosphere. The "C" stands for cooling, i.e., positive SWC and
588 LWC represent cooling of the atmospheric column. In CESM2, positive longwave
589 radiative fluxes are upwards, so LWC is calculated as the net LW radiation at the
590 TOA minus that at the surface. In CESM2, positive shortwave radiative fluxes are
591 downwards, so SWC is calculated as the net SW radiation at the surface minus the
592 net SW radiation at the TOA (or equivalently, the negative of the net SW radiation
593 at TOA minus that at the surface). Both terms are positive for cooling (energy
594 loss). SH is the downwards sensible heat flux at the surface (i.e., positive values
595 indicate atmospheric cooling). H is estimated as the residual between L_cP and Q.
596 In the global mean, the circulation term (i.e., H) is zero, implying $L_cP = Q$. As Q is
597 composed of LWC and SWC (and SH but it is generally small), this balance shows
598 that condensational heating via precipitation is largely balanced by radiative
599 cooling of the atmosphere. An increase in atmospheric SW absorption (e.g., via
600 CH_{4SW}) will decrease atmospheric radiative cooling and in turn, decrease
601 precipitation.

602 Figure 5a,b shows the atmospheric energy budget decomposition for the total, fast
603 and slow responses under 10xCH$_{4SW}$ and 2.5xCH$_{4SW}$. Under both CH$_{4SW}$
604 perturbations, the decrease in global mean precipitation (i.e., the energy of
605 precipitation L$_c$P) is dominated by the slow response. For example, under
606 2.5xCH$_{4SW}$ L$_c$P decreases by -0.09 ± 0.09 W m^{-2} under the fast response. This
607 increases (in magnitude) to -0.15 ± 0.30 W m^{-2} under the slow response (i.e.,
608 total decrease is -0.24 ± 0.28 W m^{-2}). Although these 2.5xCH$_{4SW}$ changes are not
609 significant at the 90% confidence level, all three L$_c$P decreases are significant
610 under 10xCH$_{4SW}$ at -0.29 ± 0.10, -0.83 ± 0.27 and -1.12 ± 0.25 W m^{-2},
611 respectively. The precipitation decrease under the slow response is largely
612 associated with a decrease in net longwave atmospheric radiative cooling (i.e.,
613 LWC) of -0.17 ± 0.34 W m^{-2} for 2.5xCH$_{4SW}$ and -1.03 ± 0.32 W m^{-2} for
614 10xCH$_{4SW}$ (i.e., anomalous longwave radiative warming) which is consistent with
615 cooling of the troposphere (e.g., Supplementary Fig. 6b and 7b). The decrease in
616 net longwave atmospheric radiative cooling under the slow response is weakly
617 muted by an increase in net shortwave radiative cooling at 0.03 ± 0.08 W m^{-2} for
618 2.5xCH$_{4SW}$ and 0.30 ± 0.09 W m^{-2} for 10xCH$_{4SW}$ (i.e., anomalous shortwave
619 radiative cooling), consistent with tropospheric cooling and decreases in
620 atmospheric water vapor (i.e., specific humidity decreases throughout the
621 troposphere under the slow response; Supplementary Fig. 6f and 7f). This yields
622 less solar absorption by water vapor, i.e., QRS decreases in the mid- and upper-
623 troposphere under the slow response (Supplementary Fig. 6a and 7a).

624 The CH$_{4SW}$ decrease in L$_c$P under the fast response is associated with opposite
625 changes in SWC and LWC, including dominance of the SWC term as opposed to
626 the LWC term. This includes a SWC decrease of -0.18 ± 0.03 W m^{-2} for
627 2.5xCH$_{4SW}$ and -0.85 ± 0.04 W m^{-2} for 10xCH$_{4SW}$ (i.e., less shortwave radiative
628 cooling), which is consistent with the enhanced solar absorption by CH$_{4SW}$ under
629 the fast response (e.g., Supplementary Fig. 6a and 7a). This is partially offset by
630 an increase in LWC, consistent with mid- to upper-tropospheric warming and
631 enhanced outgoing longwave radiation.

632 The L$_c$P decrease under the total response is associated with similar magnitude
633 decreases in both SWC and LWC. This is particularly true for 10xCH$_{4SW}$, where
634 the SWC term decreases by -0.55 ± 0.08 W m^{-2} and the LWC term decreases by
635 -0.51 ± 0.30 W m^{-2}. Under 2.5xCH$_{4SW}$, the corresponding changes are $-0.15 \pm$
636 0.07 and -0.08 ± 0.33 W m^{-2}, respectively. In all cases, the H term is near zero in
637 the global mean (i.e., energy transport in global mean should be zero). Similarly,
638 the SH term is generally small in all cases.

639   To summarize these results, the decrease in global mean precipitation under CH_{4SW}
640   is associated with both the fast and slow response, with most of the precipitation
641   decrease related to the slow (surface temperature mediated) response. The
642   decrease in precipitation under the fast response is largely due to the enhanced
643   solar absorption by CH_{4SW} (decrease in the SWC term above), i.e., as atmospheric
644   solar absorption increases, net atmospheric radiative cooling decreases, which
645   leads to a decrease in precipitation. In contrast, the decrease in precipitation under
646   the slow response is largely due to cooling of the troposphere and a decrease in net
647   longwave atmospheric radiative cooling (decrease in the LWC term above).
648
649   The importance of both the fast and slow response (and the dominance of the slow
650   response) in driving less global mean precipitation under CH_{4SW} is in contrast to
651   other shortwave absorbers such as black carbon. With idealized black carbon
652   perturbations, for example, the fast and slow global mean precipitation responses
653   oppose one another. The fast response (associated with black carbon atmospheric
654   solar absorption) yields a global mean decrease in precipitation whereas the weaker
655   slow response (associated with surface warming) yields an increase in global mean
656   precipitation (Samset et al., 2016; Stjern et al., 2017). The net result is a decrease
657   in global mean precipitation, largely due to the fast response and enhanced
658   atmospheric solar absorption by black carbon.

659   This difference in behavior between BC and CH_{4SW} is because BC has a positive
660   TOA ERF whereas CH_{4SW} has a negative TOA ERF. The positive TOA ERF
661   under BC acts to warm the surface, which promotes an increase in precipitation
662   under the slow response. The negative TOA ERF under CH_{4SW} acts to cool the
663   surface (as shown here), which promotes a decrease in precipitation under the slow
664   response. However, both BC and CH_{4SW} have a positive atmospheric ERF (which
665   promotes less precipitation via fast adjustments).

666   Thus, the main difference between the black carbon and CH_{4SW} impact on global
667   mean precipitation is related to the slow response. Black carbon warms the surface
668   which mutes the overall decrease in global mean precipitation (from the fast
669   response). In contrast, CH_{4SW} cools the surface, which adds to the overall decrease
670   in global mean precipitation (and contributes more to the decrease than does the
671   fast response).

672   We further decompose the global mean precipitation response based on the
673   equation $L_c\Delta P = A + \eta\Delta TAS$ (e.g., Fläschner et al., 2016) where L_c is defined above
674   (and equal to 29 W m^{-2} (mm day^{-1})$^{-1}$); ΔP is the change in the global mean
675   precipitation [mm day^{-1}]; ΔTAS is the change in global mean near-surface air

676   temperature [K]; A is an adjustment term (estimated from our fSST experiments)
677   that accounts for the change in precipitation independent of any change in surface
678   temperature [W m^{-2}], which can be further decomposed into SWC+LWC+SH,
679   where SWC is the net shortwave radiative cooling of the atmosphere as defined
680   above [W m^{-2}] ; LWC is the net longwave radiative cooling of the atmosphere as
681   defined above [W m^{-2}]; and SH is the downwards sensible heat flux at the surface
682   [W m^{-2}] (positive values for these three terms indicate cooling and energy loss; as
683   defined above). The hydrological sensitivity parameter is η [W m^{-2} K^{-1}].

684   Supplementary Table 3 (and Supplementary Figure 8) shows that the hydrological
685   sensitivity parameter is always larger (in magnitude) under the various SW+LW
686   signals (e.g., 2.5xCH$_{4LW+SW}$) as compared to the LW-only signal (e.g., 2.5xCH$_{4LW}$).
687   The SW signal consistently (outside of 2.5xCH$_{4SW}$) yields the smallest η.
688   However, η has a relatively large uncertainty and it is not significantly different
689   between the various SW+LW signals and the corresponding LW-only signals. For
690   example, the hydrological sensitivity parameter is 2.47 ± 0.24 W m^{-2} K^{-1} for
691   10xCH$_{4LW+SW}$ and 2.39 ± 0.16 W m^{-2} K^{-1} for 10xCH$_{4LW}$. The corresponding value
692   for 10xCH$_{4SW}$ is 2.24 ± 0.73 W m^{-2} K^{-1}. Thus, although there are systematic
693   differences, the hydrological sensitivity parameter is not significantly different
694   under the LW-only effects versus SW effects of CH$_4$.

695   **3.6 Comparisons with CO$_{2SW}$**
696
697   In addition to CH$_4$, other greenhouse gases (GHGs), including carbon dioxide
698   (CO$_2$), also absorb solar radiation. As with most climate models, CESM2 (via
699   RRTMG) includes a representation of CO$_2$ SW absorption. In particular, RRTMG
700   includes CO$_2$ SW absorption in four NIR/mid-IR bands: 1.3-1.6 μm, 1.9-2.15 μm,
701   2.5-3.1 μm and 3.8-12.2 μm. As mentioned above, RRTMG underestimates CO$_2$
702   SW IRF by 25-45% (Hogan and Matricardi, 2020).

703   Prior studies (focused on the radiative forcing) have shown the SW absorption
704   effects of the present-day CO$_2$ perturbation are relatively small (Myhre et al., 1998;
705   Etminan et al., 2016; Shine et al., 2022). For example, from the perspective of the
706   SARF at the tropopause, CO$_2$ SW absorption yields a negative forcing that acts to
707   decrease the magnitude of the CO$_2$ LW forcing by about 5% (Myhre et al., 1998;
708   Etminan et al., 2016). This is largely due to direct SW absorption in the
709   stratosphere dominating over relatively weak increases in tropospheric SW
710   absorption due to overlap with water vapor (Etminan et al., 2016). The former acts
711   to decrease downward SW at the tropopause (leading to a negative contribution
712   that dominates the net effect), whereas the latter decreases upwards SW at the

713   tropopause (leading to a smaller, positive forcing). The direct SW absorption in
714   the stratosphere, by reducing LW cooling, also affects the temperature adjustment
715   (i.e., the LW flux from the stratosphere to the troposphere is increased). As shown
716   by Etminan et al. (2016), the overall negative contribution due to CO_{2sw} is due to
717   the dominance of its 2.7 μm band. In contrast, for CH_{4sw}, the overall positive SW
718   forcing is due to both its 1.7 and 2.3 μm bands. This contrasting behavior between
719   CO_{2SW} and CH_{4SW} is largely driven by the amount of overlap of the SW absorption
720   bands with the near-IR absorption bands for water vapor (Etminan et al., 2016).
721

722   To gain a better understanding of the importance of the SW absorption effects due
723   to CH_4 relative to CO_2, we repeat our suite of CESM2 experiments, but based on
724   idealized CO_2 perturbations, including 2x and 4x preindustrial atmospheric CO_2
725   concentrations. This includes two sets of identical experiments (e.g., Table 1), one
726   that includes CO_2 LW+SW radiative effects (e.g., $2xCO_2^{EXP}$) and one that lacks
727   CO_2 SW radiative effects (e.g., $2xCO_{2NOSW}^{EXP}$). CO_2 SW absorption in the four
728   NIR/mid-IR bands in RRTMG is turned off in the simulations that lack CO_2 SW
729   radiative effects. These are compared to the default preindustrial control
730   experiment (PIC^{EXP}), which includes CO_2 (and CH_4) LW+SW radiative effects, as
731   well as to a new preindustrial control experiment with CO_2 SW radiative effects
732   turned off (i.e., LW effects only, denoted as $PIC_{NOCO2SW}^{EXP}$). As with the methane
733   perturbations, this suite of CO_2 simulations allows quantification of the CO_2
734   LW+SW, LW and SW radiative effects, denoted for example as $2xCO_{2LW+SW}$,
735    $2xCO_{2LW}$ and $2xCO_{2SW}$. The $2xCO_{2LW+SW}$ signal is obtained by subtracting the
736   default $2xCO_2$ perturbation from the default control ($2xCO_2^{EXP} - PIC^{EXP}$). The
737    $2xCO_{2LW}$ signal is obtained by subtracting the $2xCO_2$ perturbation without CO_2
738   SW absorption from the corresponding control simulation without CO_2 SW
739   absorption ($2xCO_{2NOSW}^{EXP} - PIC_{NOCO2SW}^{EXP}$). The $2xCO_{2SW}$ signal is obtained by
740   taking the double difference, i.e., $(2xCO_2^{EXP} - PIC^{EXP}) - (2xCO_{2NOSW}^{EXP} -$
741    $PIC_{NOCO2SW}^{EXP})$.

742   We note here that it is difficult to directly compare our CH_4 and CO_2 results. For
743   example, 2.5xCH_4 represents an increase of ~0.0012 ppm whereas 2xCO_2
744   represents an increase of ~560 ppm. Nonetheless, we provide a qualitative
745   comparison below.

746   Figure 6 shows the corresponding TOA radiative fluxes and rapid adjustments for
747   both 2xCO_2 and 4xCO_2 (Supplementary Figure 9 shows the 4xCO_{2sw} radiative flux
748   decompositions for the total, fast and slow response). As expected, these
749   perturbations yield a large positive TOA LW IRF at 2.59 ± 0.05 W m^{-2} for 2xCO_2

750 and 5.30 ± 0.05 W m^{-2} for 4xCO$_2$. The corresponding TOA SW IRFs are also
751 positive, but they are much smaller at 0.03 ± 0.05 and 0.05 ± 0.05 W m^{-2},
752 respectively. The total rapid adjustment for both CO$_2$ perturbations is negative
753 under SW radiative effects at -0.06 ± 0.08 W m^{-2} for 2xCO$_2$ and -0.40 ± 0.09
754 W m^{-2} for 4xCO$_2$. The larger negative total ADJ offsets the less positive IRF,
755 leading to a negative ERF at -0.03 ± 0.15 W m^{-2} for 2xCO$_{2SW}$ and -0.35 ± 0.15
756 W m^{-2} for 4xCO$_{2SW}$ (only the latter is significant at the 90% confidence level). We
757 reiterate that these negative values are due to isolation of CO$_2$ shortwave
758 absorption alone; CO$_2$'s longwave effects still dominate the total rapid adjustment
759 and ERF. Recall that under CH$_4$, the shortwave effects dominate the total SW+LW
760 rapid adjustment but not the ERF (Fig. 1).

761 These results are qualitatively consistent with 2.5xCH$_{4SW}$ (Fig. 1), including a
762 negative ADJ that offsets the positive IRF, leading to a negative ERF. The
763 methane SW radiative effect, however, represents a larger percentage of its LW
764 radiative effect. As discussed above, CH$_{4SW}$ offsets ~20% of the positive ERF
765 associated with CH$_{4LW}$ (although not significant under 2.5xCH$_4$). This is due to a
766 relatively strong negative rapid adjustment associated with CH$_{4SW}$ (e.g., $-0.16 \pm$
767 0.10 W m^{-2} for 2.5xCH$_{4SW}$, which increases to -0.77 ± 0.11 W m^{-2} for
768 10xCH$_{4SW}$). This, in turn, drives the negative CH$_{4SW}$ ERF.

769 In contrast, 2xCO$_{2SW}$ and 4xCO$_{2SW}$ offset only 0.7% and 4%, respectively (only the
770 latter is significant at the 90% confidence level), of the positive ERF associated
771 with their LW radiative effects. The weaker CO$_{2SW}$ muting of CO$_{2LW}$ ERF is
772 related to a relatively weak CO$_{2SW}$ negative adjustment (-0.06 ± 0.08 W m^{-2} for
773 2xCO$_{2SW}$, but increasing to -0.40 ± 0.09 W m^{-2} for 4xCO$_{2SW}$), that leads to a
774 relatively weak negative CO$_{2SW}$ ERF. The weaker CO$_{2SW}$ muting of CO$_{2LW}$ ERF is
775 also related to the relatively large and positive CO$_{2LW}$ ERF. This large and positive
776 CO$_{2LW}$ ERF is due to a relatively large and positive ADJ under CO$_{2LW}$ (largely due
777 to the stratospheric temperature adjustment, as well as clouds; Fig. 6) which
778 reinforces the relatively large and positive CO$_{2LW}$ IRF. For example, 2xCO$_{2LW}$
779 yields an ADJ of 1.55 ± 0.08 W m^{-2} and a corresponding ERF of 4.15 ± 0.10 W
780 m^{-2}. Thus, the weaker CO$_{2SW}$ muting of CO$_{2LW}$ ERF is related to a relatively weak
781 SW radiative effect, particularly compared to its very strong LW radiative effect.

782 We also note that the negative total rapid adjustment due to CO$_2$ SW absorption is
783 dominated by a negative stratospheric temperature adjustment (Fig. 6c,d). This is
784 also in contrast to methane, where clouds (followed by the stratospheric
785 temperature adjustment) drive most of the negative total rapid adjustment under
786 SW radiative effects (Fig. 1b). For 4xCO$_{2SW}$, the stratospheric adjustment is

787 -0.46 ± 0.01 W m^{-2} as compared to -0.19 ± 0.07 W m^{-2} for clouds. This larger
788 negative stratospheric adjustment under $4xCO_{2SW}$ is consistent with relatively large
789 shortwave heating above ~200 hPa (to be discussed below).

790 The ERF, IRF and ADJ under $2xCO_2$ LW+SW radiative effects shown here
791 compare well with those from PDRMIP (Smith et al., 2018), although CESM2
792 yields a larger positive ADJ (and ERF). For example, PDRMIP yields a multi-
793 model mean IRF, ERF and ADJ of ~2.5, 3.7 and 1.2 W m^{-2}, respectively. The
794 corresponding values from our $2xCO_2$ CESM2 simulation are 2.6 ± 0.06, $4.1 \pm$
795 0.11 and 1.6 ± 0.07 W m^{-2}. The bulk of CESM2's larger ADJ is due to a larger
796 cloud adjustment at 0.98 ± 0.05 W m^{-2} compared to 0.45 W m^{-2} for PDRMIP.

797 Figure 7a shows the global mean instantaneous shortwave heating rate profile for
798 $2xCO_{2SW}$ and $4xCO_{2SW}$. Both profiles show a decrease in QRS throughout the
799 troposphere with two minima, one near 800 hPa in the lower-troposphere and
800 another near 250 hPa in the upper troposphere. Above 200 hPa, QRS increases
801 rapidly through the stratosphere, reaching ~0.15 K d^{-1} at 3.6 hPa under $4xCO_{2SW}$.
802 The vertical structure of QRS under CO_{2SW} shows similarities to that under CH_{4SW}
803 (Fig. 2a), but CO_{2SW} exhibits QRS decreases throughout the entire troposphere as
804 well as relatively large QRS increases in the stratosphere. In other words, the
805 transition level from decreasing to increasing QRS occurs higher aloft under
806 CO_{2SW}, with larger QRS increases in the stratosphere.

807 The corresponding fSST 'fast' responses are included in Figure 7b-f. The QRS
808 profile (Fig. 7b) is very similar to the corresponding instantaneous profile (Fig. 7a).
809 The relatively large CO_{2SW} stratospheric solar heating helps to explain the
810 correspondingly large negative stratospheric temperature adjustment (Fig. 6c,d).
811 That is, the large increase in stratospheric solar absorption leads to corresponding
812 warming and subsequently, enhanced outgoing longwave radiation which acts to
813 cool the climate system. The decrease in tropospheric QRS is associated with
814 weak cooling (Fig. 7c), and increases in both relative humidity (Fig. 7d) and clouds
815 (Fig. 7e), with stronger responses under $4xCO_{2SW}$ as compared to $2xCO_{2SW}$. The
816 opposite responses occur in the stratosphere. These results again share similarities
817 to those based on CH_{4SW} (Fig. 2), but CO_{2SW} exhibits more uniform changes
818 throughout the troposphere (i.e., the transition level occurs higher aloft), as well as
819 relatively large stratospheric changes.

820 Due to the relatively weak and non-significant $2xCO_{2SW}$ radiative fluxes (and
821 limited computational resources), we only perform the coupled ocean-atmosphere
822 simulations for $4xCO_2$. Figure 8a-c shows the global mean total, fast and slow
823 response vertical profiles under $4xCO_{2SW}$ for QRS, temperature and cloud cover.

824 Significant cooling (Fig. 8b) occurs under the total (and slow) response throughout
825 the troposphere, with maximum cooling of ~0.5 K near 200 hPa under the total
826 response. Above this level, cooling gradually weakens and transitions into
827 warming aloft, peaking at ~1 K near 50 hPa. The corresponding vertical CLOUD
828 total response profile (Fig. 8c) shows increasing cloud cover throughout the
829 troposphere, with decreases aloft (near 100 hPa), generally similar to the fast
830 response but with larger tropospheric CLOUD increases and weaker CLOUD
831 decreases aloft. The global maps of the TAS and P total climate response under
832 $4xCO_{2SW}$ are included in Figure 8d,e. $4xCO_{2SW}$ drives a significant decrease in
833 TAS and P at -0.38 ± 0.12 K and -0.031 ± 0.01 mm d^{-1} (-1.05%).

834 Supplementary Table 2 (and Supplementary Figure 3d) show the individual
835 components of the TOA energy decomposition equation, including the estimated
836 climate feedback parameter, for the $4xCO_2$ simulations. As with the methane
837 signals, the climate feedback parameter is larger (in magnitude) under $4xCO_{2LW+SW}$
838 as compared to $4xCO_{2LW}$, but not significantly so. For example, α is -1.18 ± 0.06
839 W m^{-2} K^{-1} for $4xCO_{2LW+SW}$ and -1.11 ± 0.06 W m^{-2} K^{-1} for $4xCO_{2LW}$. The
840 corresponding α value for $4xCO_{2SW}$ is -0.31 ± 0.93 W m^{-2} K^{-1}.

841 Under $4xCO_{2SW}$, the TAS and P responses are quite small as compared to the
842 corresponding LW radiative effects at 5.84 ± 0.08 K and 0.27 ± 0.01 mm d^{-1}
843 (9.1%), respectively. For example, if CH_{4LW} yielded the same 5.84 K of warming,
844 this would correspond to surface cooling associated with CH_{4SW} of ~1.75K
845 (assuming 30% offset, which may not apply here). In terms of TAS, $4xCO_{2SW}$
846 mutes 6.5% of the warming due to LW radiative effects. For P, $4xCO_{2SW}$ mutes
847 11.5% of the increase in precipitation due to LW radiative effects. Thus, the
848 muting effects of CO_{2SW} are much weaker than those associated with CH_{4SW}, where
849 ~30% of the warming and ~60% of the wetting due to CH_4 LW radiative effects
850 are offset.

851 We also perform the atmospheric energy balance calculation (Section 3.5) on the
852 suite of $4xCO_{2SW}$ simulations (Fig. 5c). Overall, the conclusions discussed in
853 Section 3.5 under $2.5xCH_{4SW}$ and $10xCH_{4SW}$ also apply under $4xCO_{2SW}$. The
854 decrease in the global mean energy of precipitation under $4xCO_{2SW}$ (-0.91 ± 0.30
855 W m^{-2} under the total response) is associated with both the fast (a non-significant
856 decrease of -0.08 ± 0.11 W m^{-2}) and slow response (-0.83 ± 0.32 W m^{-2}). Here,
857 nearly all of the precipitation decrease (91% as opposed to 63% for $2.5xCH_{4SW}$ and
858 74% for $10xCH_{4SW}$) is related to the slow (surface temperature mediated) response.
859 In other words, only 9% of the precipitation decrease under $4xCO_{2SW}$ is due to the
860 fast response, which is much lower than that under CH_{4SW} (26-37%). The weaker

861 contribution to the decrease in total precipitation by the $4xCO_{2SW}$ fast response is
862 consistent with similar (but opposite signed) changes in the SWC and LWC terms
863 at -0.41 ± 0.04 W m^{-2} and 0.35 ± 0.12 W m^{-2}, respectively, which neutralize one
864 another. This cancellation is consistent with the $4xCO_{2SW}$ solar heating profile
865 (e.g., Fig. 7b) where nearly all of the heating occurs in the stratosphere. Thus, the
866 added solar heating—although decreasing the SWC term—primarily warms the
867 stratosphere where the energy is efficiently radiated back to space (i.e., the SWC
868 decrease is primarily balanced by an increase in the LWC term). This is in contrast
869 to the QRS profiles under CH_{4SW} (e.g., Fig. 2b) which show significant solar
870 absorption throughout the mid- and upper troposphere (pressures < 700 hPa).
871 Thus, we suggest the relatively weak decrease in precipitation under the $4xCO_{2SW}$
872 fast response (relative to the CH_{4SW} perturbations) is related to differences in the
873 vertical QRS profile, with CO_{2SW} solar absorption primarily occurring in the
874 stratosphere.

875 Supplementary Table 3 (and Supplementary Figure 8d) show the individual
876 components of the alternate precipitation energy decomposition equation,
877 including the estimated hydrological sensitivity parameter, for the $4xCO_2$
878 simulations. For example, η is 2.47 ± 0.04 W m^{-2} K^{-1} for $4xCO_{2LW+SW}$ and $2.46 \pm$
879 0.04 W m^{-2} K^{-1} for $4xCO_{2LW}$. The corresponding η value for $4xCO_{2SW}$ is smaller
880 (but not significantly so, as with methane) at 2.31 ± 0.89 W m^{-2} K^{-1}. Thus, similar
881 to the methane simulations, although there are systematic differences, we do not
882 find significant differences between the hydrological sensitivity parameter under
883 the LW-only effects versus the SW effects of CO_2.

884 **3.7 Climate Feedbacks**

885 As discussed above, the climate feedback parameter (as estimated via a regression
886 approach; Supp. Table 2) is always larger (in magnitude) under the various
887 SW+LW signals (e.g., $2.5xCH_{4LW+SW}$) as compared to the LW-only signal (e.g.,
888 $2.5xCH_{4LW}$). Although these differences are not significant, they suggest the
889 climate system does not have to warm as much to offset the same TOA energy
890 imbalance when SW effects are included. We perform an alternate procedure to
891 calculate the total climate feedback and its components by normalizing the slow
892 response's radiative flux decomposition (based on the radiative kernel method) by
893 the corresponding change in global mean near-surface air temperature. Figure 9
894 shows the corresponding feedback decomposition. We first point out that the total
895 climate feedback as calculated here (α_k) is similar (i.e., error bars overlap except
896 for $4xCO_2$) to that previously estimated using the regression approach (α) (Supp.
897 Table 2). Thus, α_k is also always larger (in magnitude) under the various

898 SW+LW signals as compared to the corresponding LW-only signals, with
899 consistently smaller (negative) magnitudes under the SW-only signals (outside of
900 2.5xCH$_{4SW}$). Although α_k has smaller uncertainty (as compared to α), these
901 differences continue to lack significance (i.e., blue bar's errors overlap in Fig. 9).
902 It is also clear, however, that the individual feedbacks (e.g., tropospheric
903 temperature feedback) are all very similar across CH$_4$ and CO$_2$ LW+SW, LW and
904 SW radiative effects—except the cloud feedback, where significant differences
905 exist (for the larger perturbations). For example, the cloud feedback is $0.05 \pm$
906 0.20 W m^{-2} K^{-1} for 10xCH$_{4LW+SW}$; 0.36 ± 0.09 W m^{-2} K^{-1} for 10xCH$_{4LW}$; and $1.0 \pm$
907 0.53 W m^{-2} K^{-1} for 10xCH$_{4SW}$ (i.e., the cloud feedback is significantly different
908 between SW versus LW radiative effects; Fig. 9a). Thus, the larger (positive)
909 cloud feedback under SW radiative effects acts to weaken the total (negative)
910 feedback, which helps to explain the previously mentioned systematically smaller
911 (in magnitude) values for α (and α_k) under SW effects. Furthermore, the
912 systematically larger (negative) values for α and α_k under SW+LW effects is due
913 to a relatively weak cloud feedback (e.g., 0.05 ± 0.20 W m^{-2} K^{-1} for
914 10xCH$_{4LW+SW)}$. We also clarify here that this weak cloud feedback under SW+LW
915 effects is due to the fact LW effects are associated with surface warming and
916 decreased low cloud cover under the slow response (Supp. Table 1), which in turn
917 drives more warming (i.e., a positive cloud feedback). This is weakened by SW
918 effects, which are associated with surface cooling and increased low cloud cover
919 under the slow response (Supp. Table 1), which in turn drives more cooling (i.e., a
920 positive feedback that opposes that under LW effects). Even though the surface
921 cooling under SW effects is relatively small compared to the warming under LW
922 effects, the cloud feedback under SW effects is larger than that under LW effects,
923 effectively leading to a smaller cloud feedback under SW+LW effects (and not
924 significant under all of the CH$_4$ perturbations). The net effect is that the planet
925 does not need warm up as much under SW+LW effects to restore energy balance,
926 due to the SW effects on clouds under the slow response (and in particular,
927 increased low clouds; Supp. Table 1). Analogously, these results imply relatively
928 large cooling per unit forcing under methane shortwave radiative effects, which in
929 turns leads to relatively less warming per unit forcing under methane shortwave
930 and longwave radiative effects.

931 The importance of low clouds is further supported by an analogous feedback
932 decomposition that separates TOA radiative fluxes into shortwave (Supplementary
933 Figure 10) versus longwave fluxes (Supplementary Figure 11). Here, the total
934 feedback (and individual feedbacks, including clouds) for TOA longwave fluxes is
935 very similar across SW+LW, LW and SW effects for each perturbation. In
936 contrast, the total feedback for TOA shortwave fluxes is more positive under CH$_4$

937 and CO_2 SW effects (significantly so for the larger perturbations), and this is
938 driven by the cloud feedback (Supp. Fig. 10). For example, the total TOA
939 shortwave flux feedback is 0.45 ± 0.21 W m^{-2} K^{-1} for 10xCH_{4LW+SW}; 0.86 ± 0.10
940 W m^{-2} K^{-1} for 10xCH_{4LW}; and 1.69 ± 0.55 W m^{-2} K^{-1} for 10xCH_{4SW}. These
941 differences are largely due to the corresponding cloud feedback at -0.14 ± 0.20
942 W m^{-2} K^{-1} for 10xCH_{4LW+SW}; 0.26 ± 0.09 W m^{-2} K^{-1} for 10xCH_{4LW}; and $1.08 \pm$
943 0.55 W m^{-2} K^{-1} for 10xCH_{4SW}.

944 Finally, we note that this cloud feedback (and its impact on the total feedback)
945 under SW effects is more important under CH_4 as opposed to CO_2 (Fig. 9d). For
946 example, although the cloud feedback is 0.85 ± 0.32 W m^{-2} K^{-1} for 4xCO_{2SW}
947 (significantly different than that for 4xCO_{2LW}), very similar values occur for
948 4xCO_{2LW+SW} (0.51 ± 0.02 W m^{-2} K^{-1}) and 4xCO_{2LW} (0.54 ± 0.03 W m^{-2} K^{-1}). This
949 is consistent with the weaker absorption of solar radiation by CO_2 (relative to
950 CH_4).

951 **4 Discussion and Conclusions**
952
953 We have expanded upon the work of A23, by explicitly simulating the radiative
954 and climate responses of the present-day (2.5x preindustrial) perturbation of
955 methane, decomposed into LW+SW, LW and SW radiative effects. Our results
956 here based on 2.5xCH_4 are consistent with the conclusions from A23, and re-
957 emphasize the importance of methane SW absorption—not only under relatively
958 large perturbations, but also under realistic, present-day perturbations (albeit with
959 larger uncertainty).
960
961 2.5xCH_{4SW} cools the surface by -0.10 ± 0.07 K whereas 2.5xCH_{4LW} warms the
962 surface by 0.35 ± 0.05 K. That is, 2.5xCH_{4SW} acts to mute 28% (7-55%) of the
963 warming due to the corresponding methane longwave radiative effects. Although
964 similar conclusions apply for precipitation, where 66% of the precipitation increase
965 associated with methane longwave radiative effects under the present-day methane
966 perturbation is offset by shortwave absorption, this muting effect is not significant
967 at the 90% confidence level (i.e., the global mean precipitation response under
968 2.5xCH_{4SW} is not significant at -0.008 ± 0.009 mm d^{-1}). Nonetheless, similar to
969 the larger methane perturbations emphasized in A23, SW absorption due to the
970 present-day CH_4 perturbation offsets ~30% of the warming and ~60% of the
971 precipitation increase associated with the present-day CH_4 LW radiative effects.
972 Muting of warming and wetting is consistent with a negative CH_{4SW} ERF due to a
973 negative rapid adjustment dominated by clouds. This in turn weakens the positive
974 ERF associated with CH_{4LW}. Under the present-day methane perturbation, ~20%

975 of the ERF associated with methane longwave radiative effects is muted by
976 shortwave absorption, which is again similar to (but not significant here) the larger
977 CH_4 perturbations in A23.
978
979 An atmospheric energy budget analysis (Fig. 5) shows that the decrease in global
980 mean precipitation under CH_{4SW} is associated with both the fast and slow response,
981 with most of the precipitation decrease related to the slow (surface temperature
982 mediated) response. The decrease in precipitation under the fast response is
983 largely due to the enhanced solar absorption by CH_{4SW}, whereas the decrease in
984 precipitation under the slow response is largely due to cooling of the
985 surface/troposphere and a decrease in net longwave atmospheric radiative cooling.
986 The importance of both the fast and slow response (and the dominance of the slow
987 response) in driving less global mean precipitation under CH_{4SW} is in contrast to
988 other shortwave absorbers such as black carbon (where the fast and slow
989 precipitation response oppose one another).
990
991 This difference in behavior (i.e., slow precipitation response) between CH_{4sw} and
992 BC comes from the different signs of the global temperature response which is
993 driven by the ERF. CH_{4SW} yields a negative ERF (Fig. 1a) and surface cooling
994 (Fig. 3f), whereas BC yields a positive ERF and surface warming (e.g., Stjern et
995 al., 2017). The former surface cooling promotes a precipitation decrease whereas
996 the latter surface warming promotes a precipitation increase. We note that the
997 different signed ERFs between CH_{4sw} and BC may (in part) be related to
998 differences in their vertical QRS profile (e.g., Allen et al., 2019). The negative
999 QRS in the lower troposphere promotes a negative low cloud adjustment for CH_{4sw}
1000 which contributes to the negative ERF. Whereas for BC (where the QRS profile is
1001 more vertically uniform with increases throughout the atmosphere e.g.,
1002 Supplementary Figure 4 from Stjern et al., 2017), the positive QRS in the lower
1003 troposphere leads to less low cloud adjustment so the ERF is overall more positive.
1004 BC is also a stronger SW absorber than is methane (i.e., in terms of its IRF), which
1005 also contributes to the larger positive ERF of BC.
1006
1007 As many climate models lack methane SW absorption, our results imply that such
1008 models may overestimate the warming and wetting due to the increase in
1009 atmospheric methane concentrations over the historical time period. Similarly,
1010 such models may also have deficient simulation of the corresponding methane
1011 climate impacts under future climate projections.
1012
1013 We further show the importance of CH_{4sw} by comparison to CO_{2sw}. CO_2 SW
1014 absorption yields qualitatively similar results to CH_4 SW absorption, including a

negative ADJ that offsets the positive IRF, leading to a negative ERF (Fig. 6; we reiterate that these negative ADJ and ERF values are due to isolation of shortwave effects alone). In contrast to CH_{4SW} (where the cloud adjustment dominates), the negative ADJ under CO_{2SW} is largely due to the stratospheric temperature adjustment, which is consistent with larger SW absorption in the stratosphere under CO_{2SW} (Fig. 7a,b). The reduced importance of the cloud adjustment under CO_{2SW} as compared to CH_{4SW} is related to differences in their vertical QRS profiles. Under CO_{2SW}, the vertical QRS profile exhibits more vertically uniform tropospheric changes (Fig. 7a-b), with the transition level from decreasing to increasing QRS occurring higher aloft (as compared to CH_{4SW}; Fig. 2a,b). These QRS differences also impact the fast precipitation response (a decrease), which is less important under CO_{2sw} as compared to CH_{4SW} (Fig. 5). Under CO_{2SW}, LWC and SWC are nearly equal and opposite in sign (leading to cancellation and small precipitation changes), whereas decreases in SWC dominate over increases in LWC under CH_{4SW}, which promotes a precipitation decrease. As most of the atmospheric solar heating under CO_{2SW} occurs in the stratosphere, this primarily warms the stratosphere where the energy is efficiently radiated back to space (i.e. the SWC decrease is primarily balanced by an LWC increase). Finally, consistent with the relatively small (negative) CO_{2sw} ERF relative to the much larger positive CO_{2LW} ERF, $4xCO_{2SW}$ muting of the $4xCO_{2LW}$ climate responses (e.g., temperature, precipitation) are also relatively small and about five times smaller as compared to the $2.5xCH_{4SW}$ muting effects.

Additional analysis of the climate feedback parameter α, climate sensitivity λ, and the hydrological sensitivity parameter η indicate consistent but non-significant differences between the LW and SW effects for both CH_4 and CO_2 (e.g., Supplementary Tables 2-3; Supplementary Figures 3 & 8). For example, SW effects (outside of $2.5xCH_{4SW}$) consistently yield smaller (negative) α values (and in turn larger positive λ); and smaller (positive) η. Again, however, these differences are not significant. An alternate procedure (based on radiative kernels applied to the slow response) to derive the climate feedback parameter and its components yields similar results, and also shows the importance of CH_{4SW} (and to a lesser extent CO_{2SW}) to the cloud feedback (Fig. 9; Supp. Fig. 10-11). In particular, SW effects lead to a stronger (positive) cloud feedback (largely due to low clouds) which effectively mutes the cloud feedback under LW effects. The leads to a more negative total climate feedback when SW effects are included, implying the climate system does not need to warm up as much to restore energy balance. Analogously, these results imply relatively large cooling per unit forcing under methane shortwave radiative effects, which in turns leads to relatively less

1054 warming per unit forcing under methane shortwave and longwave radiative effects.

1055

1056 Such potential differences in these parameters under SW versus LW effects
1057 deserves additional analysis. For example, it would be interesting to repeat some
1058 of our simulations (particularly the larger perturbations) over a longer integration
1059 time-period (e.g., 150+ years), which would help increase the signal to noise ratio.
1060 Moreover, one could reassess the above climate parameters using alternative
1061 procedures, e.g., a "Gregory"-style regression methodology (Gregory et al., 2004).
1062 Similar simulations with multiple models would also be useful.

1063

1064 As our conclusions continue to be derived from one climate model, we encourage
1065 additional multi-model studies to evaluate the robustness of these results. Ideally,
1066 this includes simulations that include interactive chemistry (e.g., methane can
1067 enhance tropospheric ozone production), as our CESM2/CAM6 simulations do not.
1068 We also reiterate that there are known deficiencies in the shortwave radiative
1069 transfer code used in most climate model calculations, including CESM2. As
1070 mentioned above, CESM2's radiative transfer model (RRTMG) underestimates
1071 CH_4 (and CO_2) SW IRF by 25-45% (Hogan and Matricardi, 2020). This is in
1072 addition to the various subtleties in the quantification of methane shortwave
1073 forcing identified by Byrom and Shine (2022). These subtleties include the need
1074 for careful representation of the spectral variation of surface albedo and the vertical
1075 profile of methane, and the role of shortwave absorption at longer wavelengths,
1076 specifically methane's 7.6 μm band that is not included in some climate model
1077 radiation codes, including RRMTG. Thus, additional efforts are needed to
1078 improve climate model representation of CH_{4SW}.

1079

1080 In the context of the most recent IPCC ERF estimates, methane SW absorption is
1081 included and is based on Smith et al. (2018). The corresponding 1750-2019 (729.2
1082 to 1866.3 ppb, or 2.6x increase) methane ERF is 0.54 ± 0.11 W m^{-2}, which includes
1083 a correction associated with methane SW absorption of -0.08 W m^{-2} (Forster et al.,
1084 2021). Our ERF estimate for 2.5xCH_4 is within this uncertainty range at $0.43 \pm$
1085 0.08 W m^{-2}. Furthermore, we estimate the CH_{4SW} correction (i.e., the CH_{4SW} ERF)
1086 at -0.10 ± 0.13 W m^{-2}, which compares very well to the IPCC estimate of -0.08
1087 W m^{-2}. We note that the IPCC estimate is based on four models, one of which is
1088 CESM1 (the predecessor to the model used here). The most recent IPCC global
1089 warming potentials (GWP) for methane (e.g., 82.5 ± 25.8 for fossil-CH_4 and a 20-
1090 year time horizon) also include methane SW absorption. Given the caveats
1091 discussed above (e.g., underestimation of CH_4 SW IRF by 25-45%), however,

1092 these estimates of the CH_{4SW} adjustment and the corresponding climate effects may
1093 be underestimated.
1094
1095 We also iterate that these are concentration ("abundance") based ERF estimates.
1096 The methane concentration used to derive such a concentration-based ERF is based
1097 on the observed change, which is influenced not only by the change in methane
1098 emissions, but also changes in emissions of other compounds that affect methane
1099 lifetime and concentrations (Stevenson et al., 2020). For example, changes in non-
1100 methane ozone precursors including nitrogen oxides and volatile organic
1101 compounds in general reduce methane concentrations. This means that the
1102 methane perturbation applied here is smaller than that which would arise if
1103 methane is emissions-driven. In the latter case, the derived methane concentration
1104 change would be higher than that observed, would take account of the impact of
1105 methane on its own lifetime, and would be attributable to the change in methane
1106 emissions alone. For example, Shindell et al. (2005) shows that the instantaneous
1107 tropopause direct radiative forcing (1998 relative to preindustrial) of methane
1108 alone increases from 0.48 to 0.59 W m^{-2}, in switching from a concentration-based
1109 to an emissions-based perspective. Accounting for the impacts of methane on
1110 ozone production and stratospheric water vapor further increases methane's
1111 radiative forcing to ~0.9 W m^{-2} (Shindell et al., 2005). A more recent estimate of
1112 the emissions-based methane ERF (including indirect effects) is 1.19$\pm$0.38 W m^{-2}
1113 (Szopa et al., 2021). This is due to indirect positive ERFs from methane enhancing
1114 its own lifetime, enhancing stratospheric water vapor, causing ozone production,
1115 and influencing aerosols and the lifetimes of hydrochlorofluorocarbons (HCFCs)
1116 and hydrofluorocarbons (HFCs) (Myhre et al., 2013; O'Connor et al., 2022). We
1117 reiterate that our simulations do not include these methane indirect effects. Such
1118 effects not only impact the ERF, but also the temperature response in the
1119 stratosphere and upper troposphere (Winterstein et al., 2019), which in turn may
1120 impact the cloud response.

1121 In conclusion, the present-day methane perturbation is associated with CH_{4SW}
1122 muting of 28% (7-55%) of the CH_{4LW} surface warming. This is consistent with the
1123 negative ERF and perhaps also a relatively strong low cloud feedback under
1124 CH_{4SW}. Despite our main conclusions, we emphasize that methane remains a potent
1125 GHG. Continued efforts to reduce CH_4 emissions are vital for staying below 1.5°C
1126 of global warming.

1127 **Code Availability**
1128

CESM2 can be downloaded from NCAR at
https://www.cesm.ucar.edu/models/cesm2/download. The Python-based radiative
kernel toolkit and the GFDL radiative kernel can be downloaded from
https://climate.rsmas.miami.edu/data/radiative-kernels/.

Data Availability

A core set of model data from the 2.5x preindustrial methane CESM2 simulations
is available here: https://doi.org/10.5281/zenodo.10357888.

Author Contributions

R.J.A performed CESM2/CAM6 simulations and analyzed the results. All authors,
including X.Z., C.A.R., C.J.S., R.J.K and B.H.S discussed the results and
contributed to the writing.

Competing Interests

The authors declare no competing interests.

Acknowledgements

References

Allen, R. J., Zhao, X., Randles, C. A., Kramer, R. J., Samset, B. H. & Smith, C. J.: Surface warming and wetting due to methane's long-wave radiative effects muted by short-wave absorption. *Nat. Geosci.*, **16**, 314-320, doi: 10.1038/s41561-023-01144-z, 2023.

Allen, R. J., Amiri-Farahani, A., Lamarque, J-F., Smith, C., Shindell, D., Hassan, T. & Chung, C. E.: Observationally-constrained aerosol–cloud semi-direct effects. *npj Clim. Atmos. Sci.*, **2**, 16, doi: 10.1038/s41612-019-0073-9, 2019.

Amiri-Farahani, A., Allen, R. J., Li, K.-F. & Chu, J.-E.: The semidirect effect of combined dust and sea salt aerosols in a multimodel analysis. *Geophys. Res. Lett.* **46**, 10512–10521, 2019.

Byrom, R. E. & Shine, K. P.: Methane's solar radiative forcing. *Geophys. Res. Lett.*, **49**, e2022GL098270, doi: 10.1029/2022GL098270, 2022.

Clement, A., Burgman, R. & Norris, J. R.: Observational and model evidence for positive low-level cloud feedback. *Science*, **325**, 460-464, 2009.

Collins, W. D., Feldman, D. R., Kuo, C. & Nguyen, N. H.: Large regional shortwave forcing by anthropogenic methane informed by Jovian observations. *Sci. Adv.* **4**, eaas9593, 2018.

Conley, A. J., Lamarque, J.-F., Vitt, F., Collins, W. D. & Kiehl, J.: PORT, a CESM tool for the diagnosis of radiative forcing. *Geosci. Model Dev.* **6**, 469–476, 2013.

Danabasoglu, G., Lamarque, J.-F., Bacmeister, D., Bailey, D. A., & et al.: The Community Earth System Model version 2 (CESM2). *J. Adv. Model. Earth Syst.* **12**, e2019MS001916, 2020.

Etminan, M., Myhre, G., Highwood, E. J. & Shine, K. P.: Radiative forcing of carbon dioxide, methane, and nitrous oxide: a significant revision of the methane radiative forcing. *Geophys. Res. Lett.* **43**, 12614–12623, 2016.

Fläschner, D., T. Mauritsen, & B. Stevens: Understanding the Intermodel Spread in Global-Mean Hydrological Sensitivity. *J. Climate*, **29**, 801–817, https://doi.org/10.1175/JCLI-D-15-0351.1, 2016.

Forster, P., T. Storelvmo, K. Armour, W. Collins, J.-L. Dufresne, D. Frame, D.J.

Lunt, T. Mauritsen, M.D. Palmer, M. Watanabe, M. Wild, and H. Zhang, 2021: The Earth's Energy Budget, Climate Feedbacks, and Climate Sensitivity. In *Climate Change 2021: The Physical Science Basis. Contribution of Working Group I to the Sixth Assessment Report of the Intergovernmental Panel on Climate Change* [Masson-Delmotte, V., P. Zhai, A. Pirani, S.L. Connors, C. Péan, S. Berger, N. Caud, Y. Chen, L. Goldfarb, M.I. Gomis, M. Huang, K. Leitzell, E. Lonnoy, J.B.R. Matthews, T.K. Maycock, T. Waterfield, O. Yelekçi, R. Yu, and B. Zhou (eds.)]. Cambridge University Press, Cambridge, United Kingdom and New York, NY, USA, pp. 923–1054, doi:10.1017/9781009157896.009.

Forster, P. M., Richardson, T., Maycock, A. C., Smith, C. J., Samset, B. H., Myhre, G., Andrews, T., Pincus, R. & Schulz, M.: Recommendations for diagnosing effective radiative forcing from climate models for CMIP6. *J. Geophys. Res. Atmos.* **121**, 12460–12475, 2016.

Gregory, J. M., Ingram, W. J., Palmer, M. A., Jones, G. S., Stott, P. A., Thorpe, R. B., Lowe, J. A., Johns, T. C. & Williams, K. D: A new method for diagnosing radiative forcing and climate sensitivity, *Geophys. Res. Lett.*, **31**, L03205, doi:10.1029/2003GL018747, 2004.

Hogan, R. J. & Matricardi, M.: Evaluating and improving the treatment of gases in radiation schemes: the Correlated K-Distribution Model Intercomparison Project (CKDMIP). *Geosci. Model Dev.* **13**, 6501–6521, 2020.

Iacono, M. J., Delamere, J. S., Mlawer, E. J., Shephard, M. W., Clough, S. A. & Collins, W. D.: Radiative forcing by long-lived greenhouse gases: calculations with the AER radiative transfer models. *J. Geophys. Res. Atmos.* **113**, D13103, 2008.

Kramer, R. J., Matus, A. V., Soden, B. J. & L'Ecuyer, T. S.: Observation-based radiative kernels from CloudSat/CALIPSO. *J. Geophys. Res. Atmos.* **124**, 5431–5444, 2019.

Li, J., Curry, C. L., Sun, Z. & Zhang, F.: Overlap of solar and infared spectra and the shortwave radiative effect of methane. *J. Atmos. Sci.* **67**, 2372-2389, 2010.

Liu, L., Shawki, D., Voulgarakis, A., Kasoar, M., Samset, B. H., Myhre, G., & et al.: A PDRMIP multimodel study on the impacts of regional aerosol forcings on global and regional precipitation. *J. Climate*, **31**, 4429-4447, 2018.

1234 Muller, C., & O'Gorman, P.: An energetic perspective on the regional response of
1235 precipitation to climate change. *Nature Climate Change* 1, 266–271, doi:
1236 10.1038/nclimate1169, 2011.

1237

1238 Myhre, G. et al., 2013: Anthropogenic and Natural Radiative Forcing. In: *Climate*
1239 *Change 2013: The Physical Science Basis. Contribution of Working Group I to the*
1240 *Fifth Assessment Report of the Intergovernmental Panel on Climate Change*
1241 [Stocker, T.F., D. Qin, G.-K. Plattner, M. Tignor, S.K. Allen, J. Boschung, A.
1242 Nauels, Y. Xia, V. Bex, and P.M. Midgley (eds.)]. Cambridge University Press,
1243 Cambridge, United Kingdom and New York, NY, USA, pp. 659–740,
1244 doi:10.1017/cbo9781107415324.018.

1245 Myhre, G, Forster, P. M., Samset, B. H., & et al., 2017: PDRMIP: a Precipitation
1246 Driver and Response Model Intercomparison Project—protocol and preliminary
1247 results. *Bull. Am. Meteorol. Soc.* **98**, 1185–1198, 2017.

1248

1249 Myhre, G., E. Highwood, Shine, K. & Stordal, F.: New estimates of radiative
1250 forcing due to well mixed greenhouse gases, *Geophys. Res. Lett.*, **25**(14), 2715-
1251 2718, doi:10.1029/98GL01908, 1998.

1252

1253 O'Connor, F. M., Johnson, B. T., Jamil, O., Andrews, T., Mulcahy, J. P., &
1254 Manners, J.: Apportionment of the pre-industrial to present-day climate forcing by
1255 methane using UKESM1: The role of the cloud radiative effect. *Journal of*
1256 *Advances in Modeling Earth Systems*, **14**, e2022MS002991,
1257 doi:10.1029/2022MS002991, 2022.

1258

1259 Pincus, R., Forster, P. M., & Stevens, B.: The Radiative Forcing Model
1260 Intercomparison Project (RFMIP): experimental protocol for CMIP6, *Geosci.*
1261 *Model Dev.*, **9**, 3447–3460, https://doi.org/10.5194/gmd-9-3447-2016, 2016.

1262 Richardson, T. B., Forster, P. M., Andrews, T. & Parker, D. J.: Understanding the
1263 rapid precipitation response to CO2 and aerosol forcing on a regional scale. *J.*
1264 *Climate*, **29,** 583–594, doi: 10.1175/JCLI-D-15-0174.1, 2016.

1265 Samset, B. H., Myhre, G., Forster, P. M., Hodnebrog, Ø., Andrews, T., Faluvegi,
1266 G, & et al.: Fast and slow precipitation responses to individual climate forcers: A
1267 PDRMIP multimodel study. *Geophys. Res. Lett.*, **43**, 2782-2791,
1268 doi:10.1002/2016GL068064, 2016.

1269

Shindell, D. T., Faluvegi, G., Bell, N. & Schmidt, G. A.: An emissions-based view of climate forcing by methane and tropospheric ozone. *Geophys. Res. Lett*., **32**, L04803, doi: 10.1029/2004GL021900, 2005.

Shine, K. P., Byrom, R. E., & Checa-Garcia, R.: Separating the shortwave and longwave components of greenhouse gas radiative forcing. *Atmospheric Science Letters*, 23(10), e1116, doi: 10.1002/asl.1116, 2022.

Smith, C. J., Kramer, R. J., Myhre, G. & et al.: Understanding rapid adjustments to diverse forcing agents. *Geophys. Res. Lett.* **45**, 12023–12031, 2018.

Smith, C. J., Kramer, R. J., Myhre, G. & et al.: Effective radiative forcing and adjustments in CMIP6 models. *Atmos. Chem. Phys.* **20**, 9591–9618, 2020.

Soden, B. J., Held, I. M., Colman, R. & et al.: Quantifying climate feedbacks using radiative kernels. *J. Clim.* **21**, 3504–3520, 2008.

Stevenson, D. S., Zhao, A., Naik, V., O'Connor, F. M., Tilmes, S., Zeng, G., Murray, L. T., Collins, W. J., Griffiths, P. T., Shim, S., Horowitz, L. W., Sentman, L. T., & Emmons, L.: Trends in global tropospheric hydroxyl radical and methane lifetime since 1850 from AerChemMIP. *Atmos. Chem. Phys*., **20**, 12905–12920, doi:10.5194/acp-20-12905-2020, 2020.

Stjern, C. W., Samset, B. H., Myhre, G., Forster, P. M. & et al.: Rapid adjustments cause weak surface temperature response to increased black carbon concentrations. *Journal of Geophysical Research: Atmospheres*. **122**, 11,462–11,481, doi:10.1002/2017JD027326, 2017.

Szopa, S., V. Naik, B. Adhikary, P. Artaxo, T. Berntsen, W.D. Collins, S. Fuzzi, L. Gallardo, A. Kiendler-Scharr, Z. Klimont, H. Liao, N. Unger, and P. Zanis, 2021: Short-Lived Climate Forcers. In *Climate Change 2021: The Physical Science Basis. Contribution of Working Group I to the Sixth Assessment Report of the Intergovernmental Panel on Climate Change* [Masson-Delmotte, V., P. Zhai, A. Pirani, S.L. Connors, C. Péan, S. Berger, N. Caud, Y. Chen, L. Goldfarb, M.I. Gomis, M. Huang, K. Leitzell, E. Lonnoy, J.B.R. Matthews, T.K. Maycock, T. Waterfield, O. Yelekçi, R. Yu, and B. Zhou (eds.)]. Cambridge University Press, Cambridge, United Kingdom and New York, NY, USA, pp. 817–922, doi:10.1017/9781009157896.008.

1306 Winterstein, F., Tanalski, F., Jöckel, P., Dameris, M., and Ponater, M.: Implication
1307 of strongly increased atmospheric methane concentrations for chemistry–climate
1308 connections. *Atmos. Chem. Phys*., **19**, 7151–7163, https://doi.org/10.5194/acp-19-
1309 7151-2019, 2019.

1311 Wood, R. & Bretherton, C. S.: On the Relationship between Stratiform Low Cloud
1312 Cover and Lower-Tropospheric Stability. *J. Climate*, **19**, 6425–6432,
1313 doi:10.1175/JCLI3988.1, 2006.

1315 Zelinka, M. D., Myers, T. A., McCoy, D. T. & et al.: Causes of higher climate
1316 sensitivity in CMIP6 models. *Geophys. Res. Lett*., **47**, e2019GL085782, 2020.

1317
1318
1319
1320
1321
1322
1323
1324
1325
1326
1327
1328
1329
1330
1331
1332
1333
1334
1335
1336
1337
1338
1339
1340
1341
1342
1343
1344
1345

Tables

Table 1. Description of CESM2/CAM6 methane and carbon dioxide experiments. Both fixed climatological sea surface temperature and coupled ocean atmosphere simulations are performed for each experiment. 2.5x preindustrial atmospheric methane concentrations represent the present-day methane perturbation which corresponds to a ~750 to ~1900 ppb increase (i.e., ~150%). Analogous experiments are conducted for $2xCO_2$ and $4xCO_2$.

Experiment	Description
$2.5xCH_4^{EXP}$	2.5xCH$_4$ with CH$_4$ LW+SW radiative effects
$2.5xCH_{4NOSW}^{EXP}$	2.5xCH$_4$ with CH$_4$ SW radiative effects turned off
PIC^{EXP}	Preindustrial CH$_4$ with CH$_4$ LW+SW radiative effects
$PIC_{NOCH4SW}^{EXP}$	Preindustrial CH$_4$ with CH$_4$ SW radiative effects turned off
Signal	**Description**
$2.5xCH_{4LW+SW} = 2.5xCH_4^{EXP} - PIC^{EXP}$	Response to CH$_4$ LW+SW radiative effects
$2.5xCH_{4LW} = 2.5xCH_{4NOSW}^{EXP} - PIC_{NOCH4SW}^{EXP}$	Response to CH$_4$ LW radiative effects
$2.5xCH_{4SW} = (2.5xCH_4^{EXP} - PIC^{EXP}) - (2.5xCH_{4NOSW}^{EXP} - PIC_{NOCH4SW}^{EXP})$	Response to CH$_4$ SW radiative effects

Figures

2.5xCH₄ Radiative Flux Components and Rapid Adjustments
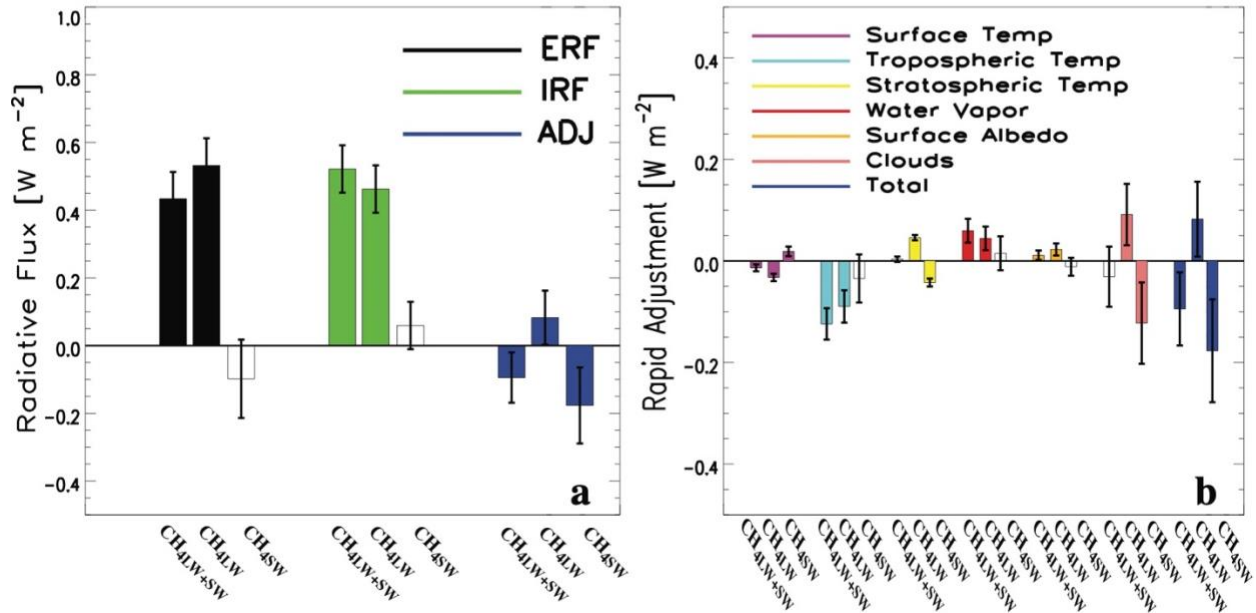
1369

1370

1371 **Figure 1. Top-of-the-atmosphere radiative flux components and rapid**
1372 **adjustments for 2.5xCH₄.** Global annual mean top-of-the-atmosphere (TOA) (a)
1373 effective radiative forcing (ERF; black), instantaneous radiative forcing (IRF;
1374 green) and rapid adjustment (ADJ; blue); and (b) decomposition of the rapid
1375 adjustment into its components including surface temperature (purple),
1376 tropospheric temperature (cyan), stratospheric temperature (yellow), water vapor
1377 (red), surface albedo (orange), cloud (pink) and total rapid adjustment (blue) for
1378 2.5xCH₄. Responses are decomposed into methane longwave and shortwave
1379 radiative effects (CH₄LW+SW), methane longwave radiative effects (CH₄LW) and
1380 methane shortwave radiative effects (CH₄SW). ERF and rapid adjustments are based
1381 on 30-year fixed climatological sea surface temperature simulations. Uncertainty
1382 is quantified using the 90% confidence interval; unfilled bars denote responses that
1383 are not significant at the 90% confidence level. Units are W m^{-2}.
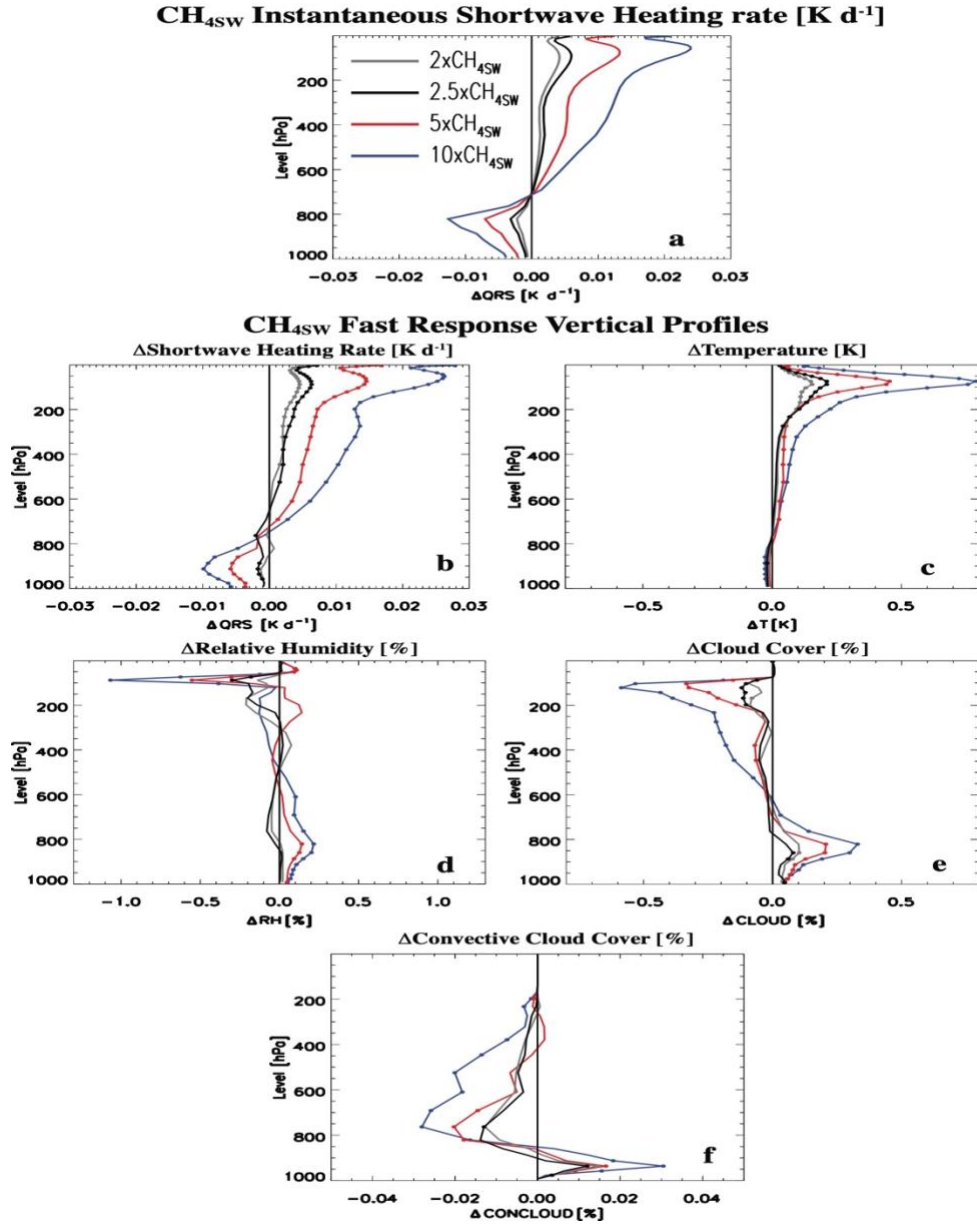
Figure 2. Global mean annual mean vertical response profiles for four CH4SW perturbations. Instantaneous (a) shortwave heating rate (QRS; units are K d^{-1}); and (b-f) fast responses of (b) QRS (units are K d^{-1}); (c) air temperature (T; units are K); (d) relative humidity (RH; units are %); (e) cloud cover (CLOUD; units are %) and (f) convective cloud cover (CONCLOUD; units are %) for 2xCH4SW (gray); 2.5xCH4SW (black); 5xCH4SW (red); and 10xCH4SW (blue). The 2xCH4, 5xCH4 and 10xCH4 simulations are from A23. A significant response at the 90% confidence level, based on a standard t-test, is denoted by solid dots in (b-f). Climatologically fixed SST simulations are used to estimate the fast responses. Instantaneous QRS profiles come from the Parallel Offline Radiative Transfer Model (PORT).

CH₄SW Total Climate Response Vertical Profiles
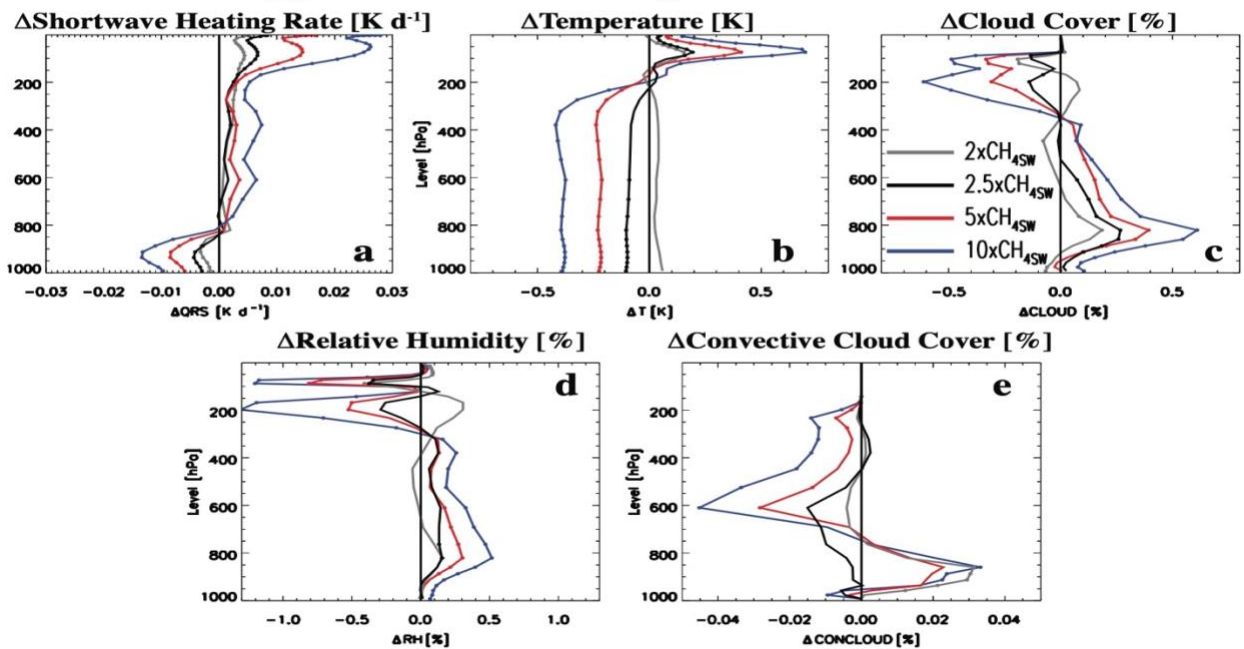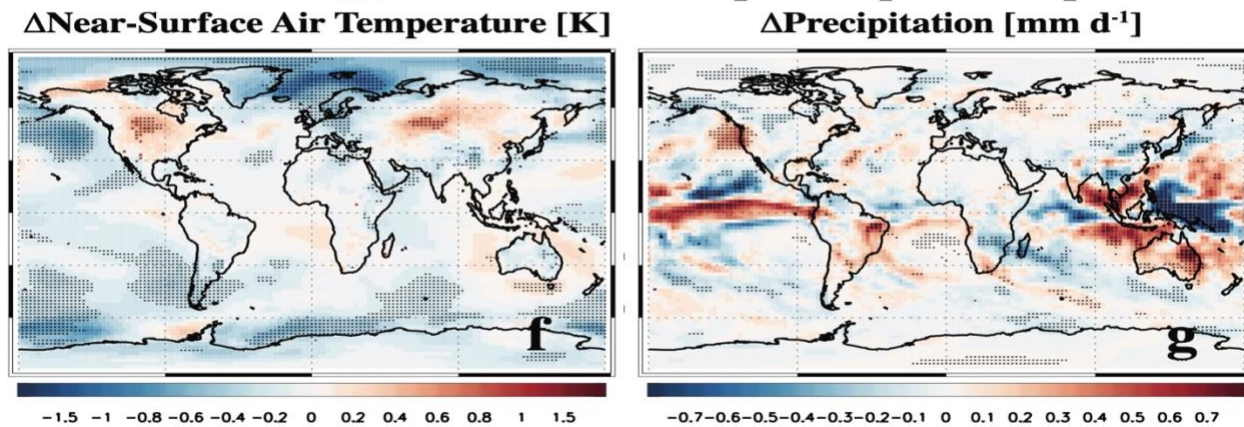
Figure 3. Total climate responses to CH₄SW. Annual mean global mean vertical response profiles of (a) shortwave heating rate (QRS; units are K d⁻¹); (b) air temperature (T; units are K); (c) cloud cover (CLOUD; units are %); (d) relative humidity (RH; units are %); and (e) convective cloud cover (CONCLOUD; units are %) for 2xCH₄SW (gray); 2.5xCH₄SW (black); 5xCH₄SW (red); and 10xCH₄SW (blue). The 2xCH₄SW, 5xCH₄SW and 10xCH₄SW simulations are from A23. Also included are global maps of the annual mean (f) near-surface air temperature [K] and (g) precipitation [mm d⁻¹] response for 2.5xCH₄SW. A significant response at the 90% confidence level, based on a standard t-test, is denoted by solid dots. Climate responses are estimated from coupled ocean-atmosphere CESM2 simulations.

2.5xCH4SW TOA Radiative Fluxes/Rapid Adjustments for the Total, Fast and Slow Response
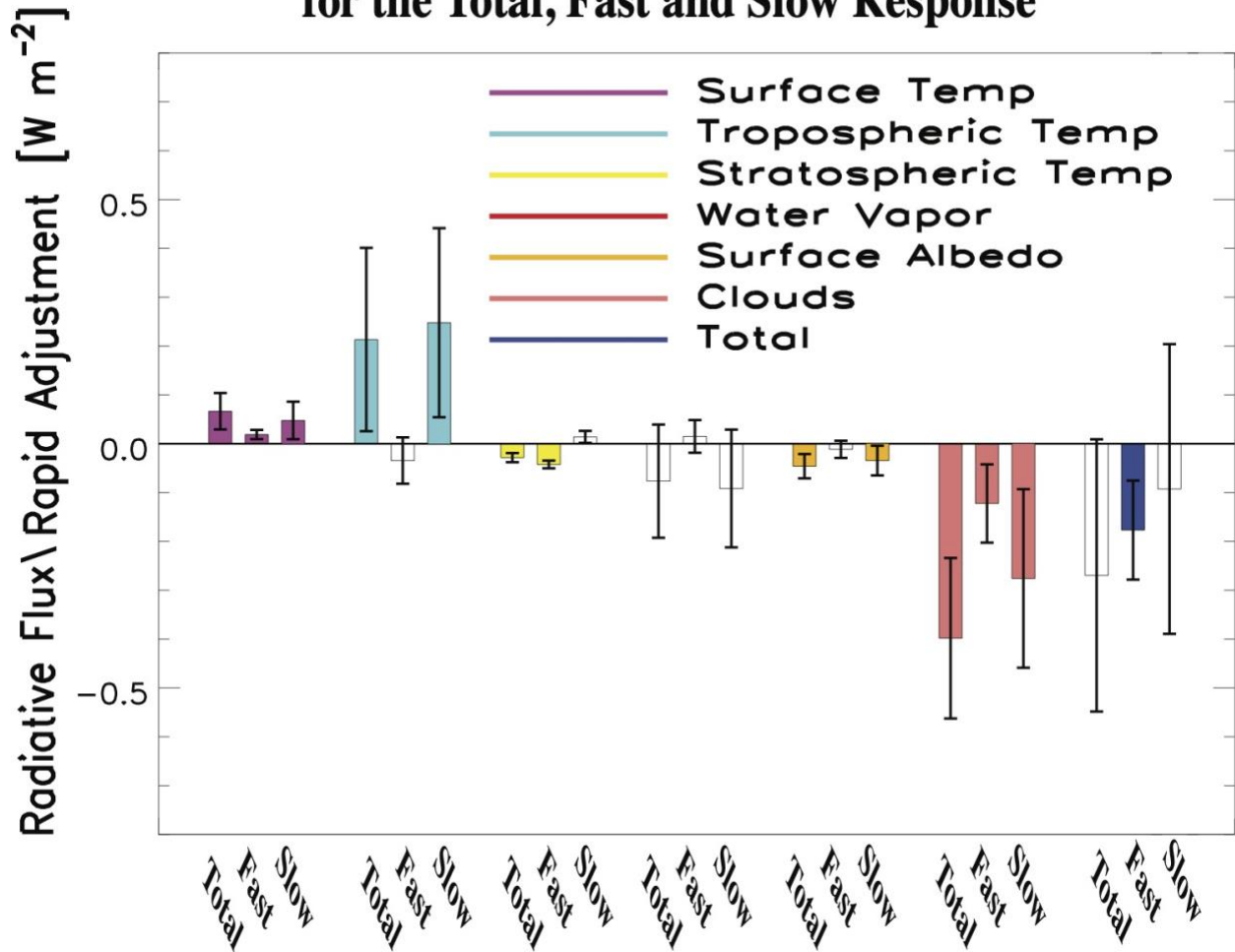
1409

Figure 4. 2.5xCH$_{4SW}$ top-of-the-atmosphere radiative flux decomposition for the total response, fast response (rapid adjustment) and slow response. Global annual mean top-of-the-atmosphere (TOA) surface temperature (purple), tropospheric temperature (cyan), stratospheric temperature (yellow), water vapor (red), surface albedo (orange), cloud (pink) and total (blue) radiative flux decomposition for 2.5xCH$_{4SW}$. The total response (from the coupled ocean atmosphere simulations) is represented by the first bar in each like-colored set of three bars; the rapid adjustment (fast response from fixed climatological sea surface temperature simulations) is represented by the second bar; and the surface-temperature-induced response (slow response; estimated as the difference of the total response minus the fast response) is represented by the third bar. Uncertainty is quantified using the 90% confidence interval; unfilled bars denote responses that are not significant at the 90% confidence level. Units are W m^{-2}.

1423
1424

**Atmospheric Energy Budget
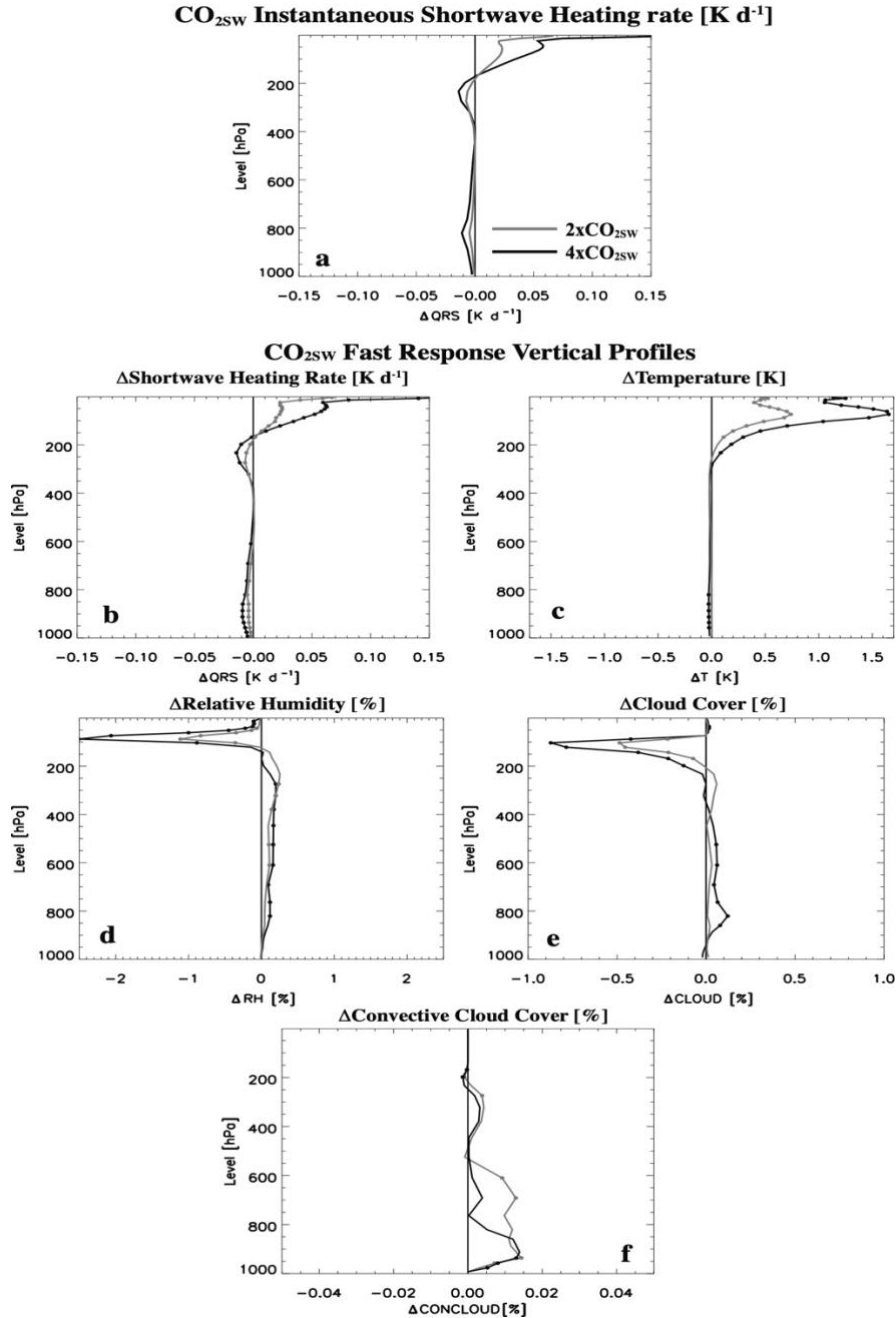for the Total, Fast and Slow Response**
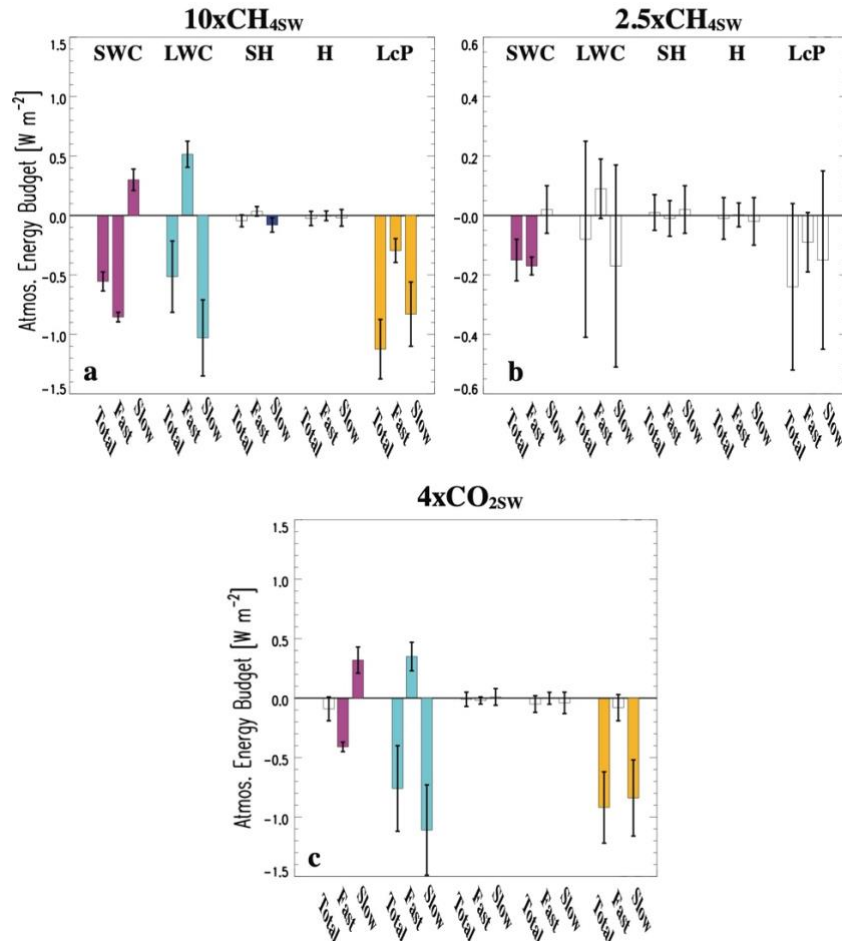
Figure 5. Atmospheric energy budget decomposition for the total, fast and slow response. Annual mean global mean energy budget decomposition for (a) 10xCH4SW; (b) 2.5xCH4SW and (c) 4xCO2SW. Components include net shortwave radiative cooling from the atmospheric column (SWC); net longwave radiative cooling from the atmospheric column (LWC); net downwards sensible heat flux at the surface (SH); and column integrated dry static energy flux divergence (H). Positive values indicate cooling (energy loss). Also included is total latent heating (LcP). The sum of the first four terms is equal to the last term (LcP). The total response (from the coupled ocean atmosphere simulations) is represented by the first bar in each like-colored set of three bars; the rapid adjustment (fast response from fixed climatological sea surface temperature simulations) is represented by the second bar; and the surface-temperature-induced response (slow response; estimated as the difference of the total response minus the fast response) is represented by the third bar. Uncertainty is quantified using the 90% confidence interval; unfilled bars denote responses that are not significant at the 90% confidence level. Units are W m^{-2}. Note the different y-axis in panel b.
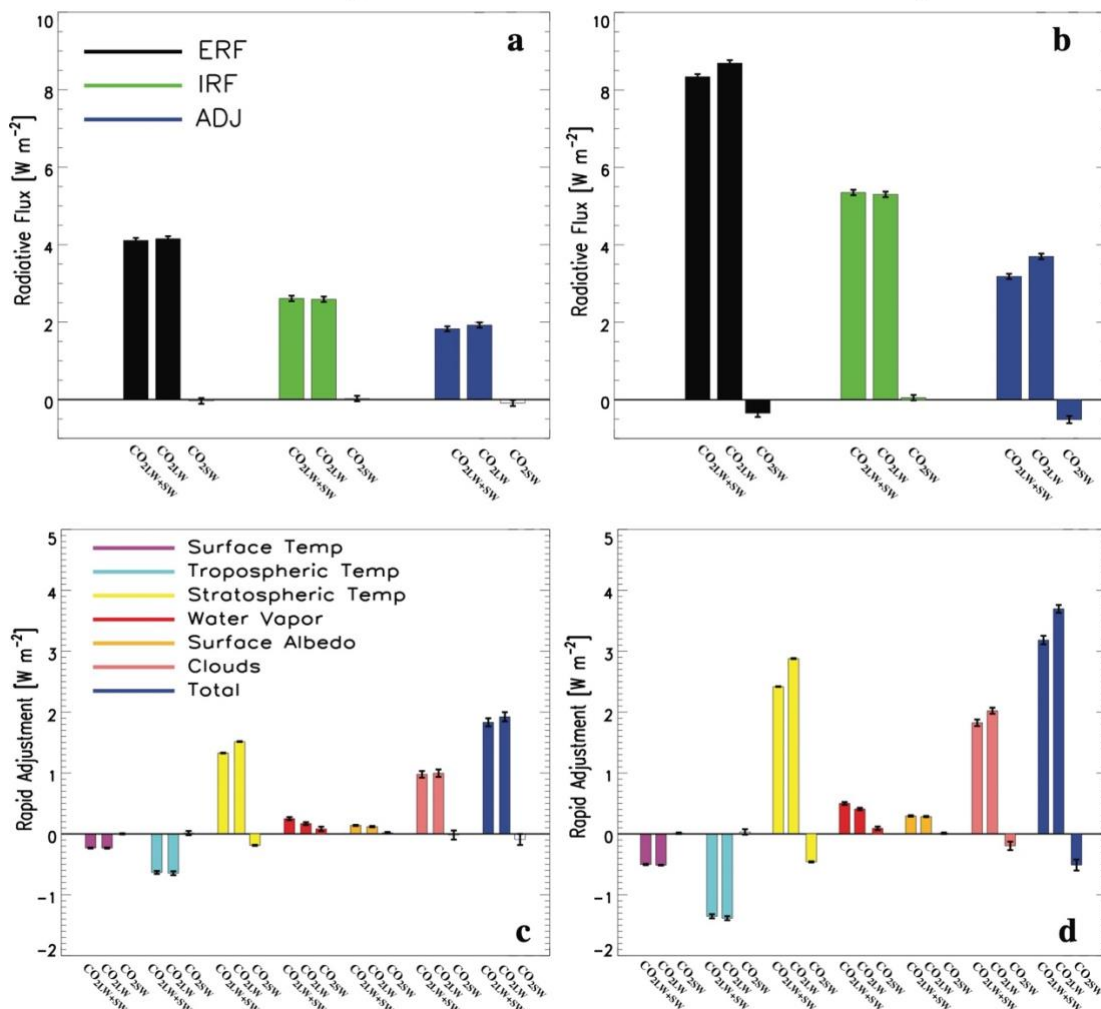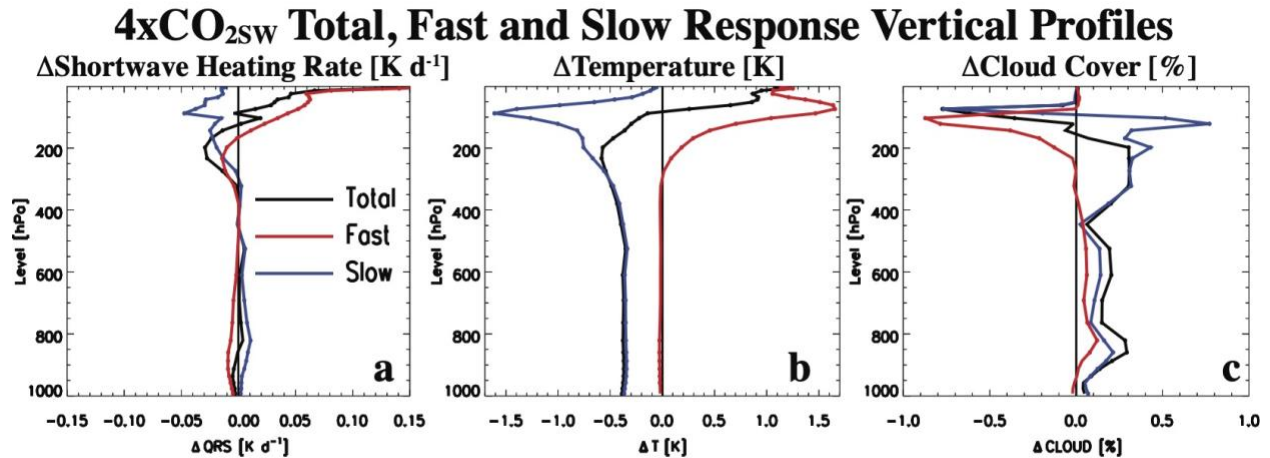
Figure 6. 2xCO₂ and 4xCO₂ top-of-the-atmosphere radiative flux components and rapid adjustments. Global annual mean TOA (a, b) effective radiative forcing (ERF; black), instantaneous radiative forcing (IRF; green) and rapid adjustment (ADJ; blue); and (c, d) decomposition of the rapid adjustment into its components including surface temperature (purple), tropospheric temperature (cyan), stratospheric temperature (yellow), water vapor (red), surface albedo (orange), cloud (pink) and total rapid adjustment (blue) for (a, c) 2xCO₂ and (b, d) 4xCO₂. Responses are decomposed into CO_2 longwave and shortwave radiative effects (CO_{2LW+SW}), CO_2 longwave radiative effects (CO_{2LW}) and CO_2 shortwave radiative effects (CO_{2SW}). ERF and rapid adjustments are based on 30-year fixed climatological sea surface temperature simulations. Uncertainty is quantified using the 90% confidence interval; unfilled bars denote responses that are not significant at the 90% confidence level. Units are W m⁻².
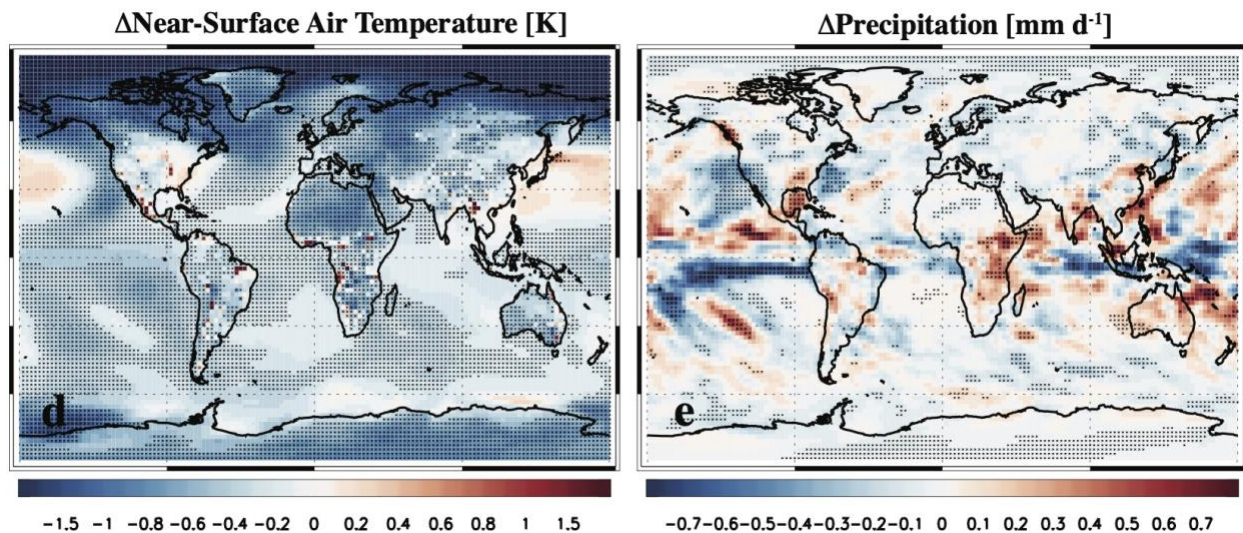
CO$_{2SW}$ Instantaneous Shortwave Heating rate [K d^{-1}]

CO$_{2SW}$ Fast Response Vertical Profiles

ΔShortwave Heating Rate [K d^{-1}]

ΔTemperature [K]

ΔRelative Humidity [%]

ΔCloud Cover [%]

ΔConvective Cloud Cover [%]

Figure 7. Global mean annual mean vertical response profiles for two CO$_{2SW}$ perturbations. Instantaneous (a) shortwave heating rate (QRS; units are K d^{-1}); and (b-f) fast responses of (b) QRS (units are K d^{-1}); (c) air temperature (T; units are K); (d) relative humidity (RH; units are %); (e) cloud cover (CLOUD; units are %) and (f) convective cloud cover (CONCLOUD; units are %) for 2xCO$_{2SW}$ (gray); and 4xCO$_{2SW}$ (black). A significant response at the 90% confidence level, based on a standard t-test, is denoted by solid dots in (b-f). Climatologically fixed SST simulations are used to estimate the fast responses. Instantaneous QRS profiles come from the Parallel Offline Radiative Transfer Model (PORT).

4xCO$_{2SW}$ Total, Fast and Slow Response Vertical Profiles

ΔShortwave Heating Rate [K d⁻¹]   **ΔTemperature [K]**   **ΔCloud Cover [%]**

4xCO$_{2SW}$ Total Climate Response Spatial Maps

ΔNear-Surface Air Temperature [K]   **ΔPrecipitation [mm d⁻¹]**

Figure 8. 4xCO$_{2SW}$ responses. 4xCO$_{2SW}$ annual mean global mean vertical response profiles of (a) shortwave heating rate (QRS; units are K d^{-1}); (b) air temperature (T; units are K); and (c) cloud cover (CLOUD; units are %) for the total (black); fast (red) and slow (blue) response. Also included are 4xCO$_{2SW}$ global maps of the annual mean (d) near-surface air temperature [K] and (e) precipitation [mm d^{-1}] change for the total climate response. A significant response at the 90% confidence level, based on a standard t-test, is denoted by solid dots. Total climate responses are estimated using from coupled ocean-atmosphere CESM2 simulations.

45

Feedback Decomposition
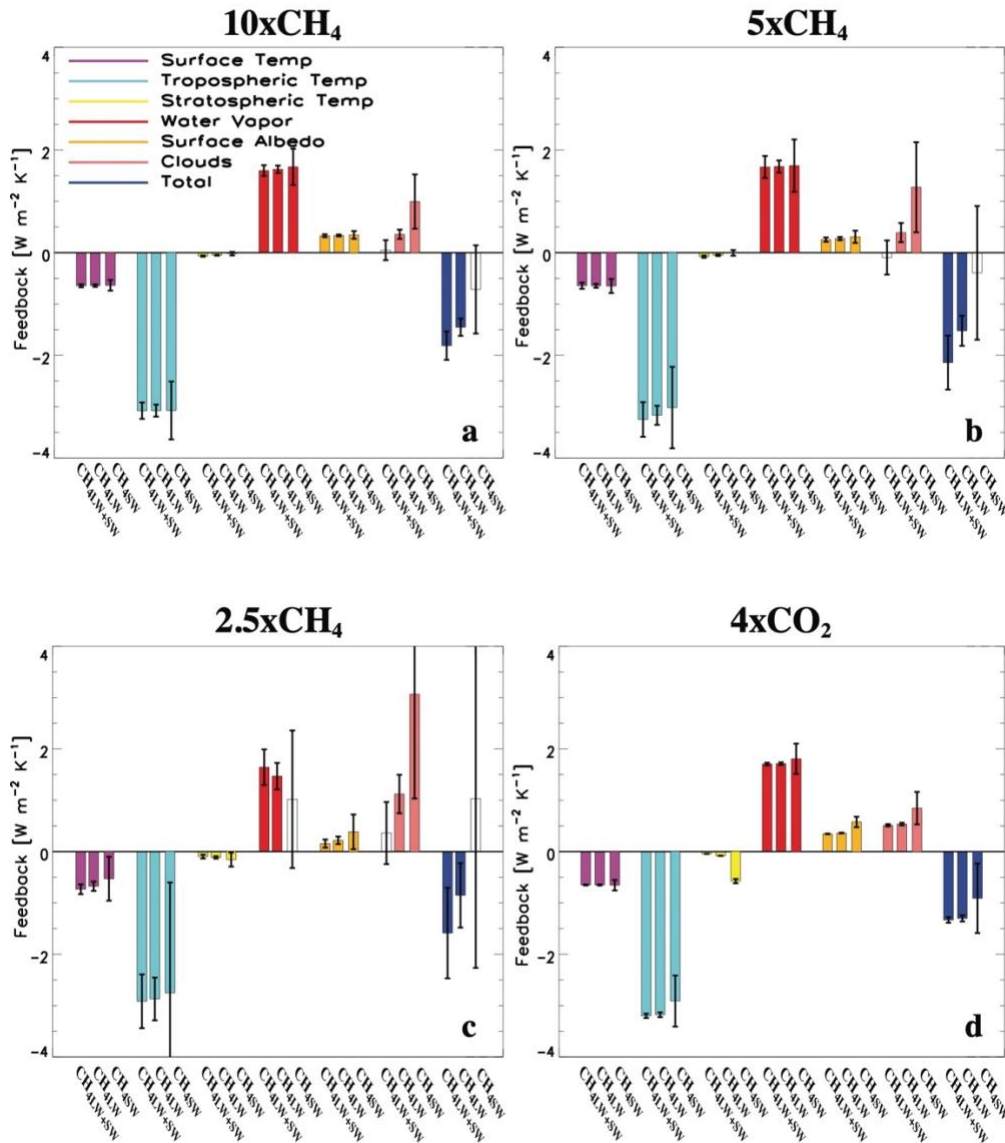
1478
1479 **Figure 9. Feedback decomposition based on the radiative kernel method.**
1480 Global annual mean top-of-the-atmosphere (TOA) surface temperature (purple),
1481 tropospheric temperature (cyan), stratospheric temperature (yellow), water vapor
1482 (red), surface albedo (orange), cloud (pink) and total (blue) feedback
1483 decomposition, as estimated by normalizing the slow response's radiative flux
1484 decomposition by the corresponding change in global mean near-surface air
1485 temperature. Feedbacks are decomposed into CH_4 and CO_2 longwave and
1486 shortwave radiative effects (e.g., CH_{4LW+SW}; first bar in each like-colored set of
1487 three bars), longwave radiative effects (e.g., CH_{4LW}; second bar) and shortwave
1488 radiative effects (e.g., CH_{4SW}; third bar). Uncertainty is quantified using the 90%
1489 confidence interval; unfilled bars denote responses that are not significant at the
1490 90% confidence level. Units are W m^{-2} K^{-1}.